Doctoral Thesis

Left-right Myosin-Is, Myosin1C, and Myosin1D exhibit distinct single molecule behaviors on the plasma membrane of *Drosophila* macrophages

Sosuke Utsunomiya

Department of Biological Sciences, Graduate School of Science

Osaka University

February 2024

Contents

1. Abstract

Left-right (LR) asymmetry is crucial for animal development, particularly in *Drosophila* where LR-asymmetric morphogenesis of organs hinges on cellular-level chirality, termed cell chirality. In this species, two class I myosins, Myosin1D (Myo1D), and Myosin1C (Myo1C), respectively determine dextral (wild type) and sinistral (mirror image) cell chirality. Previous studies demonstrated Myo1D's ability to propel F-actin in leftward circles during in vitro gliding assays, suggesting its mechanochemical role in defining dextral chirality. Conversely, Myo1C propels F-actin without exhibiting LR-directional preference in this assay, suggesting at other properties governing sinistral chirality. Given the interaction of Myo1D and Myo1C with the membrane, I hypothesized that differences in their membrane behaviors might be critical in dictating their dextral or sinistral activities. In this study, employing single-molecule imaging analyses, I investigated the dynamic behaviors of Myo1D and Myo1C on the plasma membrane. Our findings revealed that Myo1C exhibits a significantly greater proportion of slow-diffusing population compared to Myo1D. Importantly, this characteristic was contingent upon both head and tail domains of Myo1C. The distinct diffusion patterns of Myo1D and Myo1C did not exert mutual influence on each other. This divergence in membrane diffusion between Myo1D and Myo1C may be crucial for dictating cell and organ chirality.

2. Introduction

2.1 Left-right asymmetry in animals

Left-right (LR) asymmetry is a fundamental characteristic that is widely observed phenomenon in the morphology and functionality across various organisms. Many organisms exhibit LR asymmetry in their internal organs and external appearance. We humans also show genetically controlled LR-asymmetry in the morphology and arrangement of our organs. The formation mechanism of LR-asymmetry formation in vertebrates and other hindgut animals has been studied extensively. For example, in the mouse (Nonaka, Shiratori, Saijoh, & Hamada, 2002; Nonaka et al., 1998; Yoshiba et al., 2012), zebrafish (Kramer-Zucker, 2005), and *Xenopus* (Schweickert et al., 2007), the LR axis is formed by water flow generated by cilia present in the early embryo. In the mouse, cilia rotate clockwise in a bowl-shaped hollow structure called the node, which is observed approximately seven-eight days after fertilization, and generate water flow to the left side of the embryo. When the non-motile cilia of the crown cells at the periphery of the node are deformed by this flow, the $Ca2^{+}$ channel Pkd2 localized there opens, activates $Ca2^{+}$ signaling and induces the expression of genes such as *Nodal* and *Lefty*. The LR-asymmetric expression of these genes forms the LR axis (Babu & Roy, 2013; Nonaka et al., 2002; Nonaka et al., 1998; Yoshiba et al., 2012). On the other hand, vertebrates other than mammals have different mechanisms of LR-asymmetry formation from the node flow. In chickens, African clawed frogs, sea urchins, and catadromous ascidians, ion channels and

ion pumps such as H^+/K^+-ATPase, H^+-V-ATPase, and Na^+/K^+-ATPase, are localized and activated LR-asymmetrically (Adams et al., 2006; Aw, Adams, Qiu, & Levin, 2008; Hibino, Ishii, Levin, & Nishino, 2006; Levin, Thorlin, Robinson, Nogi, & Mercola, 2002; Shimeld & Levin, 2006). This occurs earlier than the LR asymmetric expression of the Nodal gene cluster. In chicken, in addition to the above mechanisms, a node-like site called the Hensen node also contributes to the formation of the LR axis. The mouse node is derived from the mesoderm, whereas the chicken Hensen node is derived from the endoderm. In addition, cilia are less mobile in the Hensen node (Cheng, D.Little, & J.Rongish, 2009; Stephen et al., 2014). The Hensen node is a LR-symmetrical structure at the beginning of its formation, but by stage 4, leftward cell migration creates a LR asymmetry (Cheng et al., 2009; Gros, Feistel, Viebahn, Blum, & Tabin, 2009). Later, as development progresses, LR-asymmetric expression of gene clusters such as *Sonic hedgehog* (*Shh*), *Fibroblast growth factor8* (*Fgf8*), and *Nodal* is induced (Gros et al., 2009). On the other hand, invertebrates such as nematodes do not have a node equivalent structure(Grand, Martín-Durán, Kenny, Truchado-García, & Hejnol, 2014). In these organisms, intracellular polarity during early development is responsible for the formation of the LR axis (Davison et al., 2016; Mech, 2014).

2.2 Cell chirality in animals

Substantial strides have been achieved in understanding the mechanisms of LR-asymmetry formation, notably in vertebrates. The underlying mechanisms of LR-asymmetric

development diverge across evolutionary lines among different species. For instance, in Lophotrochozoans and Medusozoans, the intrinsic chirality of cells emerges as a crucial factor in LR-asymmetry formation (Hozumi et al., 2006; Inaki, Liu, & Matsuno, 2016; Kuroda, Endo, Abe, & Shimizu, 2009; Spéder, Ádám, & Noselli, 2006; Wood, 1991). Object incapable of superimposing onto their mirror images are deemed chiral. This concept is exemplified in pond snails and nematodes, where the chirality of blastomeres in early embryos defines the overall body chirality (Davison et al., 2016; Kuroda et al., 2009). In *Drosophila*, the intrinsic chirality of cells induces LR-directional rotations in organs, such as the hindgut and male genitalia (Coutelis et al., 2013; Hozumi et al., 2006; Sato et al., 2015; Spéder et al., 2006). Moreover, this intrinsic cell chirality has been observed across various eukaryotic cells, spanning from slime molds to humans, termed as "cell chirality" (Tamada, Kawase, Murakami, & Kamiguchi, 2010; Tee et al., 2015; Wan & Vunjak-novakovic, 2011; Yamanaka & Kondo, 2015). The detection of cell chirality encompasses various aspects, including the chirality in cell shape, cell migration direction, intracellular dynamics, and arrangement of multiple cells (Cheng et al., 2009; Fan et al., 2018; Tee et al., 2015; Xu et al., 2007).

2.3 Myo1D and Myo1C plays crucial role in chirality formation in *Drosophila*

The formation mechanisms behind cell chirality have begun to be understood. For example, regulators of F-actin, such as Formin and actinin, play essential roles in the formation of

cell chirality (Chougule et al., 2020; Tee et al., 2023, 2015). In *Drosophila*, *Myosin1D* (*Myo1D*) and *Myosin1C* (*Myo1C*) define the enantiomeric states of cell chirality (Figure 1) (Hatori et al., 2014; Ishibashi et al., 2019; Lebreton et al., 2018; Taniguchi et al., 2011). Belonging to the evolutionarily conserved Myosin I family, both Myo1D and Myo1C possess a single head that interacts with F-actin and contribute to various cellular functions, including membrane trafficking, dynamics, and organization, facilitated through their association with the membrane via their tail domains (McIntosh & Ostap, 2016). Myo1D and Myo1C induce dextral (right-handed) and sinistral (left-handed) cell chirality, respectively, consequently influencing the corresponding LR asymmetry of organs (Hatori et al., 2014; Ishibashi, Inaki, & Matsuno, 2020; Lebreton et al., 2018; Taniguchi et al., 2011). As a molecular bases of cell chirality, it has been observed that Myo1D propels F-actin with a right-handed curvature in *in vitro* gliding assay (Lebreton et al., 2018). In this assay, Myo1C suppresses the chiral F-actin propulsion activity of Myo1D, partially explaining the sinistral activity of Myo1C (Lebreton et al., 2018). However, the misexpression of *Myo1C* induces sinistral chirality even in tissues where *Myo1D* is not involved in LR-asymmetry formation (Lebreton et al., 2018). Nevertheless, Myo1C propels F-actin without a specific LR directional preference (Lebreton et al., 2018). Thus, if the chiral turning of F-actin by Myo1D plays some roles in the formation of dextral cell chirality, Myo1C should have some other specific features that explain its role in establishing sinistral cell chirality. To address this possibility, extensive analyses of mechanochemical properties *in vitro* have revealed differences between Myo1D and

Myo1C in kinetics, such as ATPase activity, F-actin binding, and transport activity (Báez-Cruz & Ostap, 2023). Despite these findings, the precise contribution of these mechanochemical differences to direct dextral (right-handed) and sinistral (left-handed) cell chirality remains unclear. Beyond the observed mechanochemical distinctions, Myo1D and Myo1C may also exhibit biochemical and biophysical variations owing to their interactions with biomembranes. This stems from the established knowledge that both Myo1D and Myo1C bind to membrane lipids through their respective tail domains (McIntosh & Ostap, 2016). Moreover, given that Myo1D and Myo1C bind to the actin cytoskeleton via their head domains, it is plausible that they also interface with the membrane skeleton through these head domains (McIntosh & Ostap, 2016). Consequently, I speculated that differences in their dynamic molecular behaviors on or near the plasma membrane might also hold significance.

2.4 Exploring single molecule behaviors of *Drosophila* myosins

To investigate these molecular behaviors at a single molecule level, single molecule imaging is a widely used approach. In *Drosophila*, cultured larval macrophages have served as a model cell for various cell biological analyses (Kochubey, Majumdar, & Klingauf, 2006; Sampson, Amin, & Couso, 2013). Manipulated genetically, these macrophages can be isolated from larvae and cultured as primary cultures for live imaging, facilitating the observation of single molecule behavior (Figure 2). Specifically, the conduct of single molecule imaging for Myo1D and Myo1C can be readily achieved by the specific

misexpression of *Myo1D* and *Myo1C* genes fused with sequences encoding the HaloTag within these macrophages. Previous high-throughput RNA sequencing analyses have indicated that endogenous *Myo1D* and *Myo1C* exhibit moderate and low expression levels, respectively, in wild-type macrophages (Cho et al., 2020). Therefore, in the present experiments, recombinant *Myo1D* and *Myo1C* genes, each tagged with a HaloTag sequence, were expressed in macrophages in which wild-type *Myo1D* and *Myo1C* were endogenously expressed. Single molecule imaging enables us to monitor protein dynamics within cells or living organisms, offering both high temporal and spatial resolutions (Matsuoka, Shibata, & Ueda, 2013; Takebayashi, Kamimura, & Ueda, 2023; Ueda, Sako, Tanaka, Devreotes, & Yanagida, 2001; Yoshioka et al., 2020). This technique allows the elucidation of various biophysical properties of target proteins, including binding kinetics and diffusion coefficients. Considering the potential involvement of Myo1D and Myo1C in membrane-associated functions, live imaging of these proteins on or near the plasma membrane is often achieved using a total internal reflection fluorescence microscopy (TIRFM). Analytical techniques for single molecule data commonly involve estimating kinetics, such as dissociation rates derived from trajectory length distributions, and extracting diffusion-related information using mean square displacement (MSD) analysis (Golan & Sherman, 2017; Michalet, 2010; Takebayashi et al., 2023).

2.5 Results summary

Our single molecule analyses revealed distinctive behaviors between Myo1D and Myo1C dynamics on the plasma membrane. Hidden Markov Model (HMM) analyses demonstrated the existence of three distinct diffusion states for both Myo1D and Myo1C. Comparison of the trajectories of HaloTag and Myosin-1s anchored to the plasma membrane suggests that slow diffusion is the characteristic trajectory of myosin. A significantly larger portion of Myo1C exhibited slow diffusion compared to Myo1D. I also found that such differences are attributable to variations in the head domains governing ATPase activities and F-actin binding, as well as the tail domains known for their interactions with the membrane. Despite the ability of Myo1C to suppress the activities of Myo1D both *in vivo* and *in vitro* (Hozumi et al., 2006; Lebreton et al., 2018), their distinct diffusion properties did not exert mutual influence. However, considering the regulatory potential of Myosin-Is through their association with the plasma membrane, the differences observed in Myo1D and Myo1C diffusion on the plasma membrane may indeed contribute to dictating their respective dextral and sinistral activities. Indeed, a correlation was found (correlation coefficient > 0.9) between the proportion of slow diffusion states, the characteristic trajectory of myosin obtained by HMM, and the LR activity (sinistral or dextral) of the protein predicted from the Drosophila hindgut phenotype.

3. Results

3.1 Myo1C exhibits constrained diffusion on plasma membrane

Drosophila Myo1D and Myo1C dictate dextral and sinistral chirality, respectively, in cells and organs. As their activities intertwine with membrane lipid interactions, any differences in their dynamics at the plasma membrane might correlate with their respective roles in defining dextral and sinistral chirality. To investigate this, I employed single-molecule imaging through TIRFM to analyze the diffusion characteristics of Myo1D and Myo1C. Recombinant genes encoding HaloTag-fused proteins, namely Myo1D-HaloTag and Myo1C-HaloTag (Figure 3), were misexpressed in larval macrophages using the UAS/GAL4 system in *Drosophila* (Zettervall et al., 2004). The genetically engineered macrophages, isolated from third instar larvae body fluid, were cultured on a glass bottom plate, providing an optimal set-up for single molecule imaging using TIRFM (Figure 2) (Kochubey et al., 2006; Sampson et al., 2013).

Prior to conducting single molecule imaging analyses, I confirmed the activities of Myo1D-HaloTag and Myo1C-HaloTag, which respectively dictate dextral and sinistral chirality *in vivo* (Figure 4). In embryos homozygous for the *Myo1D* null mutant, $Myo1D^{L152}$, the hindgut exhibited an LR inversion frequency of 90%. Notably, *UAS-Myo1D-HaloTag* partially suppressed the LR-inversion phenotype even without a GAL4 driver in this mutant, presumably due to reported leaky expression of *UAS-Myo1D-HaloTag* (Hozumi et

al., 2008). However, hindgut-specific misexpression of *UAS-Myo1D-HaloTag* driven by *byn-GAL4* almost entirely rescued the LR-inversion phenotype in $Myo1D^{L152}$ homozygotes. Collectively, these findings suggest that Myo1D-HaloTag maintains the wild-type activity of Myo1D. Conversely, it is established that misexpression of wild-type Myo1C in the hindgut epithelium induces LR inversion of the hindgut in wild-type embryos (Hozumi et al., 2006; Spéder et al., 2006). Thus, specifically misexpressing UAS-Myo1C-HaloTag in the wild-type hindgut, driven by *byn-GAL4*, confirmed the observed LR-inversion phenotype (Figure 4). In contrast, embryos carrying UAS-Myo1C-HaloTag without *byn-GAL4* did not display the LR-inversion phenotype (Figure 4). These results indicate that Myo1C-HaloTag maintains the wild-type activity of Myo1C.

For all single molecule analyses detailed in this study, samples were independently prepared three times, and a minimum of 10 cells were observed for each sample preparation. To visualize the HaloTag-fused proteins, I used tetramethylrhodamine (TMR) ligands. Employing TIRFM, single molecule imaging was conducted at 45 frames per second (FPS) for 20 s (900 frames) per cell. After the imaging, image preprocessing, particle detection, and particle linking were performed using TrackMate (Ershov et al., 2022). Notably, our methodology did not assume particle merging or splitting, as Myo1C and Myo1D, both being type I myosins, function as monomers. To enhance tracking robustness against noise, trajectory data with tracked duration <2 frames were excluded. Furthermore, in this study, I used Myristoylated HaloTag (Myr-HaloTag) as controls to

assess protein diffusion at the plasma membrane (Kohl et al., 2014). Myristoylation serves as an anchoring mechanism, facilitating the binding of proteins to the plasma membrane.

Representative snapshots extracted from single molecule time-lapse recordings depicted discernible bright spots corresponding to individual Myo1D-HaloTag, Myo1C-HaloTag, and Myr-HaloTag proteins (Figure 5). The trajectories of tracked particles were color-coded based on the displacement distance between successive frames (Figure 5). Higher magnification images illustrating these trajectories are shown (Figure 5, A'-C'). Our tracking analysis revealed distinct behaviors: Myo1D-HaloTag and Myr-HaloTag demonstrated patterns consistent with free diffusion, whereas Myo1C-HaloTag exhibited notably reduced mobility. Many particles representing Myo1C-HaloTag appeared confined or trapped (Figure 5, A''-C'').

To characterize the dynamics of these proteins at the plasma membrane, I quantified and compared the dissociation rates of Myr-HaloTag, Myo1D-HaloTag, and Myo1C-HaloTag (Table 2 and Figure 6). Our analysis involved fitting the dissociation curve with a mixture of exponential functions (Loffreda et al., 2017; Matsuoka et al., 2013; Takebayashi et al., 2023; Yoshioka et al., 2020), which represents a complementary cumulative distribution function (1 − CDF) of tracked durations. The dissociation curve was well-fitted by a mixture of two exponential functions, rather than a single exponential function. Dissociation rates serve as a measure of the strength of the interaction between the molecule and the cell membrane. Accordingly, the exponential functions representing

higher and lower dissociation rates are denoted as short and long binding states, respectively. The proportion of long binding states was calculated as 0.25 ± 0.03, 0.32 ± 0.02, and 0.24 ± 0.03 (mean ± s.d, standard deviation) for Myo1D-HaloTag, Myo1C-HaloTag, and Myr-HaloTag, respectively (Figure 6 B). Consequently, the proportion of short binding state is 1 – the proportion of long binding states (Figure 6 B). For the short binding states, the dissociation rates were determined as 15.75 ± 1.19, 15.72 ± 1.48, and 14.28 ± 0.48 (1/s) (mean ± s.d.) for Myo1D-HaloTag, Myo1C-HaloTag, and Myr-HaloTag, respectively (Figure 6 C). Meanwhile, the dissociation rates for the long binding states were measured as 1.55 ± 0.40, 1.43 ± 0.07, and 1.85 ± 0.15 (1/s) (mean ± s.d.) for Myo1D-HaloTag, Myo1C-HaloTag, and Myr-HaloTag, respectively (Figure 6 C). Comparing these values revealed no significant difference between Myo1D-HaloTag and Myo1C-HaloTag in terms of dissociation rates. However, a significant difference was observed in the proportions between Myo1C-HaloTag and Myr-HaloTag, suggesting that Myo1C exhibits a tendency to remain at the plasma membrane for longer durations compared with proteins such as Myr, which is assumed to undergo free diffusion.

Another crucial parameter characterizing protein behavior on the plasma membrane is protein diffusivity, often evaluated using MSD as a statistical measure (Golan & Sherman, 2017; Michalet, 2010). In instances of random diffusion such as Brownian motion, the MSD typically exhibits a linear increase with the frame interval (Golan & Sherman, 2017; Michalet, 2010). However, there exist anomalous diffusions where the MSD does not

follow a linear trend (Golan & Sherman, 2017; Sabri, Xu, Krapf, & Weiss, 2020). In our comparison of MSD, I observed that Myo1D-HaloTag and Myr-HaloTag displayed a linear increase, indicative of a Brownian diffusion (Figure 7). In contrast, the MSD for Myo1C-HaloTag exhibited a change in slope at a frame interval of 2 frames (0.044 s), suggesting deviation from simple Brownian diffusion (Figure 7). This alteration was likely attributable to a higher proportion of immobilized molecules within the trajectories of Myo1C-HaloTag (Figure 5, C-C''). I assessed the diffusion coefficients of each protein by fitting the MSD curve. While the MSD function of Brownian motion was employed for Myo1D-HaloTag and Myr-HaloTag, the MSD function characterizing confined diffusion was applied to Myo1C-HaloTag (Saxton & Jacobson, 1997). The determined diffusion coefficients (D_{MSD}) were 0.226 ± 0.061, 0.455 ± 0.256, and 0.487 ± 0.051 ($\mu m^2/s$) (mean ± s.d.) for Myo1D-HaloTag, Myo1C-HaloTag, and Myr-HaloTag, respectively (Figure 7). When comparing the D_{MSD} of Myo1D-HaloTag and Myr-HaloTag, it became evident that Myo1D-HaloTag exhibited significantly lower diffusion. Although Myo1D-HaloTag appeared to be diffusing freely (Figure 5, B' and B''), it may still have been inhibited by certain factors. In contrast, Myo1C-HaloTag exhibited a significantly higher standard deviation in its D_{MSD} compared to the other proteins, rendering it incomparable with their values. This may be due to the dependence of the fitting on the initial values or differences in the shapes of the MSD functions characterizing confined diffusion and Brownian motion.

3.2 Myo1D and Myo1C exhibit distinct diffusion states

MSD analysis computes the average diffusivity from the trajectory data. It is recognized that various proteins display multiple diffusion states within the cell membrane and cytoplasm (Golan & Sherman, 2017; Janczura et al., 2021; Matsuoka et al., 2013; Sabri et al., 2020; Takebayashi et al., 2023; Yanagawa et al., 2018). Consistent with this, a naive maximum likelihood estimation with a single displacement probability density function failed to adequately describe the experimental data, implying the presence of multiple diffusion states (1 state: Figure 9, 2s state: Figure 10). Consequently, I employed HMM analysis to extract more detailed diffusion information beyond average diffusion dynamics (Takebayashi et al., 2023; Yanagawa et al., 2018). The parameters of HMM were estimated utilizing the Baum-Welch algorithm and Viterbi algorithm was used to assign the estimated states to the displacement sequences (Bishop, 2006; Rabiner, 1989). HMM serves as a probabilistic model that assumes unobserved latent variables transitioning stochastically (Bishop, 2006; Rabiner, 1989). In the context of single-molecule diffusion, these concealed states may correspond to distinct diffusion behaviors. The model comprises two primary components: hidden states and observations. Hidden states encapsulate the various diffusion behaviors that are not directly observable. Using the Baum-Welch algorithm, I estimated essential parameters such as initial states, transition probabilities between states, and distribution parameters characterizing the mobility of Myo1 (Bishop, 2006).

Using the parameters derived from the Baum-Welch algorithm, I generated probability density functions based on experimental data and those obtained via HMM analysis (Figure 11). Notably, the weights plotted in the HMM do not represent initial state probability but rather signify the steady-state probability, calculated from the initial state probability and the transition matrix. To determine the most suitable number of states in the HMM, I employed the Akaike Information Criterion (AIC) as a guiding metric (Table 3) (Akaike, 1974). In this study, I explored one to three-state models due to the failure of the Baum-Welch algorithm to converge models comprising four or more states. Remarkably, the three-state model exhibited the minimum AIC across Myo1D-HaloTag, Myo1C-HaloTag, and Myr-HaloTag datasets (Sub figure of Myo1D, Myo1C, and Myr in Figure 13). These three distinct diffusion states were categorized as follows: slow diffusion state, middle diffusion state, and fast diffusion state, based on the respective values of the diffusion coefficient. The parameters estimated by the Baum-Welch algorithm were used to assign states to the displacement series by the Viterbi algorithm (Figure 12) (Forney, 1973). The slow diffuse state (blue) appears to be tethered to something or stuck in place. The middle diffuse state in Myo1D has a displacement similar to the fast diffuse state, while in Myo1C the middle diffuse state (brown) has a displacement similar to the slow diffuse state. In Myo1C, however, the middle diffuse state (brown) has a similar displacement to the slow diffuse state. This may also indicate that Myo1D and Myo1C actually have diffusion states that are closer to the two states. Since the fast diffusion state was more abundant in Myr, which is expected to diffuse most freely with few interactions with other

proteins (see below for detailed analysis), I expect that the characteristic state for myosin is the slow diffusion state. This is consistent with the ability of myosin to bind F-actin.

To discern distinctive diffusion characteristics in the movement of Myo1D-HaloTag, Myo1C-HaloTag, and Myr-HaloTag on the plasma membrane, I conducted a comparative analysis of the proportion of diffusion states and the associated diffusion coefficients (D_{HMM}) (Table 4 and Figure 14). Our findings revealed that Myo1C-HaloTag exhibited a notably higher proportion of slow diffusion states compared with Myo1D-HaloTag and Myr-HaloTag (Myo1D-HaloTag: 0.353 ± 0.038, Myo1C-HaloTag: 0.609 ± 0.031, Myr-HaloTag: 0.414 ± 0.060). Conversely, it displayed a considerably lower proportion of fast diffusion states than both Myo1D-HaloTag and Myr-HaloTag (Myo1D-HaloTag: 0.20 ± 0.08, Myo1C-HaloTag: 0.06 ± 0.00, Myr-HaloTag: 0.33 ± 0.09). These findings indicated that the estimated D_{HMM} of the fast diffusion state was highest for Myo1C-HaloTag. However, the majority of Myo1C-HaloTag molecules displayed slower diffusion, surpassing the percentages observed for both Myo1D-HaloTag and Myr-HaloTag (Figure 14; Figure 15). The aforementioned conclusions align with the results of the MSD analysis, demonstrating that Myo1C-HaloTag exhibited a confined diffusion-like MSD curve (Figure 7). This finding is consistent with the parameters derived from the Baum-Welch algorithm.

3.3 Differences in diffusion properties among Myo1C and Myo1D were attributed to their head and tail domains

Considering that Myo1C and Myo1D showed distinct properties in diffusion states at the plasma membrane, I next explored the domains responsible for these differences. Type I myosins consist primarily of two crucial domains: the head and tail domains (Morgan, Skovronsky, Artavanis-Tsakonas, & Mooseker, 1994). The head domain is pivotal for interactions with F-actin (McIntosh & Ostap, 2016), and the tail domain is essential for interactions with the plasma membrane (McIntosh & Ostap, 2016). To delve into whether these domains contribute to differential behavior of Myo1C and Myo1D on the plasma membrane, I expressed *UAS-Myo1Dtail-HaloTag* and *UAS-Myo1Ctail-HaloTag*, encoding only the tail domains of Myo1D and Myo1C, respectively, tagged with HaloTag in larval macrophages (Figure 3). In addition, chimeric genes were constructed, incorporating combinations of Myo1D and Myo1C head and tail domains—*UAS-Myo1D head-Myo1C IQtail-HaloTag* and *UAS-Myo1C head-Myo1D IQtail-HaloTag*—and expressed under similar conditions (Figure 3). Prior to single molecule imaging, I confirmed that these deletion-mutant genes and chimeric genes retained their expected roles in LR-asymmetric development *in vivo*. *In vivo* studies confirmed that hindgut-specific misexpression of *UAS-Myo1D-HaloTag* by *byn-GAL4* largely rescued the LR-inversion phenotype in $Myo1D^{L152}$ homozygotes (Figure 4). However, misexpression of *UAS-Myo1Dtail-HaloTag* under the same conditions failed to rescue the LR inversion (Figure 16), because the head domain of

Myo1D is required for its dextral activity, as shown before (Hozumi et al., 2008; Lebreton et al., 2018). Conversely, hindgut-specific misexpression of *UAS-Myo1D head-Myo1C IQtail-HaloTag* by *byn-GAL4* significantly rescued the LR-inversion phenotype in $Myo1D^{L152}$ homozygotes. Introducing *UAS-Myo1D head-Myo1C IQtail-HaloTag* into $Myo1D^{L152}$ homozygotes in the absence of a GAL4 driver partially suppressed their LR-inversion phenotype, attributable to the previously documented phenomenon of leaky expression found in UAS strains (Figure 16) (Hozumi et al., 2008). These findings align with prior evidence that dextral chirality is specified through the head domain of Myo1D, not the tail domain (Hozumi et al., 2008; Lebreton et al., 2018). Similarly, hindgut-specific misexpression of *UAS-Myo1C-HaloTag* in wild-type embryos induced LR inversion of the hindgut (Figure 4). Misexpression of *UAS-Myo1Ctail-HaloTag* under the same conditions failed to induce this phenotype (Figure 16), confirming that sinistral chirality is specified through the head domain, not the tail domain, of Myo1C (Hozumi et al., 2008; Lebreton et al., 2018). Moreover, hindgut-specific misexpression of *UAS-Myo1C head-Myo1D IQtail-HaloTag* in wild-type embryos induced LR inversion, whereas *UAS-Myo1C head-Myo1D IQtail-HaloTag* without *byn-GAL*4 did not induce LR inversion (Figure 16). Therefore, the *in vivo* behaviors of these four genes aligned with predictions from previous studies.

To elucidate the dynamics of these proteins on the plasma membrane, I conducted further quantification of dissociation rates (Table 2, Figure 17, and Figure 18). A comparative analysis between full-length Myo1C-HaloTag and Myo1Ctail-HaloTag revealed a

significant reduction in the proportion of the long binding state for the tail domain of Myo1C in contrast to full-length Myo1C (Myo1C: 0.32 ± 0.02, Myo1Ctail: 0.18 ± 0.02). This finding strongly implies that the head domain of Myo1C contributes to prolonged binding to the plasma membrane. Additionally, dissociation rate analysis revealed that Myo1Ctail-HaloTag exhibited significantly higher dissociation rates in both short and long binding states compared with Myo1C-HaloTag (Figure 19). However, in the case of Myo1D, deletion of its head domain (Myo1Dtail-HaloTag) did not yield any noticeable impact on either the proportion of binding states or their dissociation rates (Figure 18 and Figure 19) . These outcomes indicate that while the head domain of Myo1C plays a pivotal role in maintaining Myo1C at the plasma membrane, the head domain of Myo1D does not significantly influence the binding of Myo1D to the plasma membrane.

Moreover, beyond the head domains, the tail domains also contribute to the diffusion behaviors of Myo1D and Myo1C on the plasma membrane. A comparative analysis between Myo1Dtail-HaloTag and Myo1Ctail-HaloTag showed that Myo1Ctail-HaloTag displayed a decreased proportion of the long binding state and exhibited higher dissociation rates in both short and long binding states (Figure 18 and Figure 19). This difference indicates a faster dissociation rate of the tail domain of Myo1C compared with that of Myo1D. These distinctions associated with the tail domains were corroborated by examining chimeric proteins between Myo1D and Myo1C, specifically, Myo1D head-Myo1C IQtail-HaloTag and Myo1C head-Myo1D IQtail-HaloTag (Figure 3). In contrast to

Myo1D-HaloTag, Myo1D head-Myo1C IQtail-HaloTag displayed a higher dissociation rate of the long binding state, akin to Myo1Ctail-HaloTag (Figure 18 and Figure 19). These findings strongly indicate that the tail domain of Myo1C dissociates from the plasma membrane more rapidly than that of Myo1D. However, Myo1C head-Myo1D IQtail-HaloTag demonstrated dissociation rates and proportions of the long and short binding states similar to Myo1C-HaloTag (Figure 18 and Figure 19). Therefore, it appears that the tail domain of Myo1C, unlike Myo1D, possesses an inherent activity that enhances the dissociation rate of the long binding state.

Our investigation extended to understanding the roles of the head and tail domains in determining the diffusional properties of Myo1D and Myo1C (Table 4, Figure 20 and Figure 21). I compared the proportion of diffusion states, as determined by HMM, among the deletion and chimeric proteins of Myo1D and Myo1C (Figure 20 A and Figure 21). Remarkably, among the three distinct diffusion states, the proportion of the fast diffusion state notably increased in Myo1Ctail-HaloTag compared with full-length Myo1C-HaloTag, suggesting a contribution of the head domain of Myo1C to a lower D_{HMM} on the plasma membrane (Figure 20 A and Figure 21). However, I did not observe such a difference between Myo1Dtail-HaloTag and full-length Myo1D-HaloTag. The D_{HMM} for the fast diffusion state were segregated into two groups based on the origin of the tail domain (Figure 20 B and Figure 21). Proteins with tail domains derived from Myo1D exhibited D_{HMM} of approximately 0.5–0.6 $\mu m^2/s$ in the fast diffusion state. Conversely, proteins with

tail domains derived from Myo1C displayed D_{HMM} exceeding 0.8 $\mu m^2/s$ in the fast diffusion state. This outcome strongly suggests that the tail domain determines the D_{HMM} of the fast diffusion state in *Drosophila* myosins. Consequently, both the head and tail domains play regulatory roles in the diffusion and dissociation dynamics of Myo1D and Myo1C. However, it was evident that the head domain of Myo1D did not influence dissociation when combined with either the tail domain of Myo1D or Myo1C.

3.4 Diffusion of Myo1D and Myo1C did not mutually influence each other

Myo1C has been identified to counter the dextral functions of Myo1D *in vivo* (Hozumi et al., 2006; Lebreton et al., 2018) and inhibit the Myo1D's activity of propelling F-actin toward the right side in an *in vitro* gliding assay when both were attached to lipids on a glass plate (Lebreton et al., 2018). Thus, it was hypothesized that Myo1D and Myo1C may mutually influence each other's behavioral traits on the plasma membrane, such as diffusion. To investigate this potential interaction, experiments were conducted manipulating the relative expression levels of Myo1D and Myo1C (Figure 22, Figure 23, Figure 24, Figure 25, Figure 26, Table 2 and Table 4). Behaviors of Myo1D-HaloTag were observed in macrophages misexpressing UAS-GFP-Myo1C or UAS-Myo1C dsRNA (double-stranded RNA of Myo1C to induce RNA interference (RNAi) against Myo1C) to modulate Myo1C expression levels. Additionally, behaviors of Myo1C-HaloTag were observed in macrophages misexpressing UAS-Myo1D-GFP or UAS-Myo1D dsRNA (RNAi against Myo1D) to adjust Myo1D expression levels. UAS-GFP and UAS-mCherry

RNAi were used as controls under the same conditions. Surprisingly, the parameters of binding states and diffusion states of Myo1D-HaloTag and Myo1C-HaloTag remained largely consistent across all conditions, although some conditions in Myo1C-HaloTag showed statistically significant differences (Figure 22, Figure 23, Figure 24, Figure 25, Figure 26, Table 2 and Table 4). However, at this stage, it is unclear what such differences mean. These findings suggest that the diffusion behaviors of Myo1D and Myo1C on the plasma membrane did not mutually influence each other.

3.5 Proportion of slow diffusion state was correlated to the phenotype of embryonic hindgut

The results of this study revealed that the proportion of slow diffusion state is one of the factors contributing to the difference in single-molecule dynamics between Myo1D and Myo1C. If the proportion of slow diffusion state reflects the difference in the activity of Myo1D and Myo1C, it should be correlated with the phenotype of the embryonic hindgut. Therefore, I defined the chirality index of each protein as expected from the phenotype of the embryonic hindgut and checked whether it correlated with the percentage of slow diffusion states. The chirality index of each protein was set to -1 for dextral direction, 1 for sinistral direction, and 0 for no direction. For example, the chirality index of full-length Myo1D is -1, Myo1Dtail is 0, and full-length Myo1C is 1. The correlation between the chirality index and the proportion of slow diffusion states showed a Pearson's correlation coefficient of 0.93 (Figure 27). Although there are some problems such as the discrete

nature of the chirality index and the fact that it is not a macrophage based phenotype, it is possible that there is a correlation between the slow diffusion state and the chirality index.

4. Discussion

4.1 Myo1D and Myo1C exhibit different single molecule dynamics

Myo1D and Myo1C exhibit distinct single-molecule dynamics at the plasma membrane of *Drosophila* third instar larval macrophages. Myo1D exhibits Brownian-like single-molecule dynamics like Myr-HaloTag, which is anchored to the plasma membrane by myristoylation. On the other hand, Myo1C exhibited single-molecule dynamics as if it were bound to something or restricted in diffusion by some factor. This feature was also evident in the MSD, where the slope of the Myo1C's MSD changed significantly and reached a plateau at a frame interval of 0.044 s. This indicates that the diffusion of Myo1C is restricted by binding or other factors. An attempt was made to compare the diffusion coefficient D_{MSD} of each protein from the MSD curves, but the standard deviation of D_{MSD} for Myo1C became so large, probably due to the curvature of the MSD for restricted diffusion, that a fair comparison between Myo1D and Myr was not possible. Since type I myosin generally binds to F-actin through its motor domain, the restricted diffusion suggested for Myo1C may reflect the difference in binding time between type I myosin and F-actin. Indeed, when the motor domain of Myo1C was deleted (Myo1Ctail), the trajectory was reduced, as often observed with Myo1C. *In vitro* biochemical measurements predicted that Myo1C would bind to F-actin longer than Myo1D, and the results obtained in this study were consistent with this.

4.2 The difference in single-molecule diffusion between Myo1D and Myo1C resulted from the difference in the proportion of diffusion state

From the HMM analysis, it was concluded that both Myo1D and Myo1C have three diffusion states in the plasma membrane of *Drosophila* cells. This result was also true for Myr. Focusing on the fraction of each diffusion state and the diffusion coefficient D_{HMM}, the results suggest that the difference in the single-molecule dynamics of each protein may be caused by the difference in the fraction of diffusion states. A study in *Dictyostelium*, using membrane proteins of different sizes, has reported that the diffusion coefficient is not determined by the diversity of the proteins, but by the viscosity of the plasma membrane as the primary determinant (Takebayashi et al., 2023). Given the comparison of the diffusion status of Myo1D, Myo1C, and Myr, it is possible that a similar phenomenon occurs in *Drosophila* cells.

4.3 The difference in the diffusion state of Myo1D and Myo1C results from the difference between the head and tail domains

I analyzed the domains responsible for the greater population of Myo1C displaying reduced diffusion compared to Myo1D along the plasma membrane. Single-molecule analyses revealed that both the head and tail domains of Myo1C exhibit characteristics that limit diffusion coefficients. However, the exact properties within these domains responsible for impeding diffusion remain unclear. Previous predictions have indicated that the attachment

of Myo1C to actin lasts approximately 9 times longer than that of Myo1D (Báez-Cruz & Ostap, 2023). Considering that myosins engage with actin through their head domains, it is plausible that the lower diffusion coefficients of Myo1C's head domain might stem from its prolonged binding to F-actin. However, the use of inhibitors to suppress the polymerization of F-actin might not be appropriate for exploring the interaction between the head domain and F-actin in diminishing Myo1C's diffusion, because they also impact various aspects of membrane dynamics and structure. In contrast, the tail domains of Myo1D and Myo1C have known affinities for distinct lipid molecules such as phosphatidylinositol 4,5-bisphosphate with varying specificities (Lebreton et al., 2018). This discrepancy in the influence of the tail domain on diffusion coefficients may be explained by their differing affinities to membrane lipids.

4.4 Single molecule dynamics of Myo1D and Myo1C were independent

In the embryonic hindgut, Myo1D defines the default LR asymmetry, and its activity is suppressed by MyoIC; increasing Myo1C expression mirrors the LR asymmetry of the embryonic hindgut. It has also been reported from an *in vitro* gliding assay that the Myo1D-induced bending properties of F-actin are altered by the amount of Myo1C. Based on these previous studies, I hypothesized that the single-molecule dynamics of Myo1D and Myo1C may be dependent on each other. The results of this study strongly suggest that Myo1D and Myo1C are independent at the plasma membrane of *Drosophila* macrophages. This is demonstrated by the fact that neither the dissociation constant nor the diffusion state

of Myo1C and Myo1D is altered when the expression level of Myo1D and Myo1C is increased or decreased in macrophages. These findings, together with the lack of opposing chiral properties found for Myo1D and Myo1C, suggest that Myo1D and Myo1C may independently regulate chirality in *Drosophila*.

4.5 Hypothesis of a link between myosins and LR asymmetry in Drosophila

I defined chirality index for each protein expected from the embryonic hindgut phenotype and examined whether it correlated with the proportion of slow diffusion states. There may be a correlation between the slow diffusion state and the chirality index. A candidate for further study would be to analyze the correlation between slow diffusion and phenotypes within macrophages. For example, human foreskin fibroblasts seeded on micropatterns and fibroblasts cultured with zebrafish melanophores show chirality of F-actin. In *Drosophila* macrophages, F-actin may also have an unknown chirality, and there are many unknowns about the molecular properties of Myo1D and Myo1C. Further research is needed to elucidate the chirality driven specifically by Myo1D and Myo1C. Recently, both the dextral activity of Myo1D and the sinistral activity of Myo1C have been reported to require actin nucleator DAAM (Chougule et al., 2020). It has been suggested that Myo1D and Myo1C independently regulate chirality in *Drosophila*, but there are also common components such as DAAM. Integrating these results with the fact that only Myo1D has the ability to bend F-actin, the following hypotheses are possible (Figure 28): Myo1D and DAAM imparts

chirality to F-actin, which is then transmitted to the plasma membrane and cytoskeleton via adhesion proteins. Myo1C transfers the DAAM-dependent F-actin chirality to the plasma membrane and cytoskeleton via adhesion proteins. In the future, I will analyze whether chirality exists in F-actin dynamics in macrophages and to investigate the relationship between actin chirality and single-molecule dynamics of myosins.

4.6 Overview

In *Drosophila*, Myo1D and Myo1C play pivotal roles in determining the enantiomorphic (dextral and sinistral) states of cell chirality, crucial for the LR asymmetry in various organs (Hozumi et al., 2006; Lebreton et al., 2018; Sato et al., 2015; Spéder et al., 2006). Investigations into origins of cell chirality revealed that Myo1D propels F-actin counterclockwise in *in vitro* gliding assays (Lebreton et al., 2018). However, Myo1C, similar to other myosins, propelled F-actin in a linear fashion (Lebreton et al., 2018). Therefore, the underlying mechanisms governing Myo1C's sinistral activity remains unknown. The sinistral activity attributed to Myo1C in cell chirality seems to involve additional complexity (Báez-Cruz & Ostap, 2023). To understand this complexity, detailed studies on the mechanochemistry of Myo1D and Myo1C were conducted *in vitro* (Báez-Cruz & Ostap, 2023). Notably, Myo1D exhibited a 12.5-fold higher actin-activated steady-state ATPase rate and an 8-fold higher MgATP release rate compared with Myo1C (Báez-Cruz & Ostap, 2023). Furthermore, analysis of vesicle transportation *in vitro* indicated that Myo1D induced robust transportation of 50-nm vesicles along F-actin through actin

binding, unlike Myo1C, which showed actin binding without vesicle transportation (Báez-Cruz & Ostap, 2023). These results suggested that Myo1C is a slow transporter with prolonged actin attachment, whereas Myo1D has kinetic properties conducive to efficient vesicle transport. Hence, the divergent kinetic properties of Myo1D and Myo1C could explain their functions in determining cell chirality (Báez-Cruz & Ostap, 2023). On the other hand, it is known that Myosin-Is interacts with biological membranes and regulates membrane trafficking, dynamics, and organization (McIntosh & Ostap, 2016). Thus, the dynamics of Myo1D and Myo1C on the plasma membrane, such as diffusion and dissociation, may also play roles in their specific contributions to directing cell chirality. Through single-molecule analyses, Ifound that Myo1C displays reduced diffusion compared to Myo1D on the plasma membrane. While the precise involvement of these distinct properties in cell chirality remains unclear, our findings propose an additional layer of regulation that might impact the activities of Myo1D and Myo1D though their intracellular behavior.

It has been long established that Myo1D and Myo1C antagonize their respective dextral and sinistral activities *in vivo* (Hozumi et al., 2006; Lebreton et al., 2018). Recent findings additionally suggest that Myo1C suppresses the activity of Myo1D to propel F-actin in a rightward direction in *in vitro* gliding assays (Lebreton et al., 2018). These results indicate a direct interference by Myo1C in the mechanochemical functions of Myo1D. However, our previous genetic analyses revealed that the sinistral activity elicited by Myo1C can be

achieved in null mutants of Myo1D, implying the capacity of Myo1C to execute its sinistral function independently of Myo1D. Hence, despite our single molecule analyses indicating no mutual influence of Myo1D and Myo1C on their diffusion properties, this observation does not preclude the possibility that their distinct diffusion characteristics within the plasma membrane might indeed contribute to defining their dextral and sinistral activities. To address this possibility, further studies on the cell biological significance of these distinct diffusion properties becomes imperative.

5. Figure

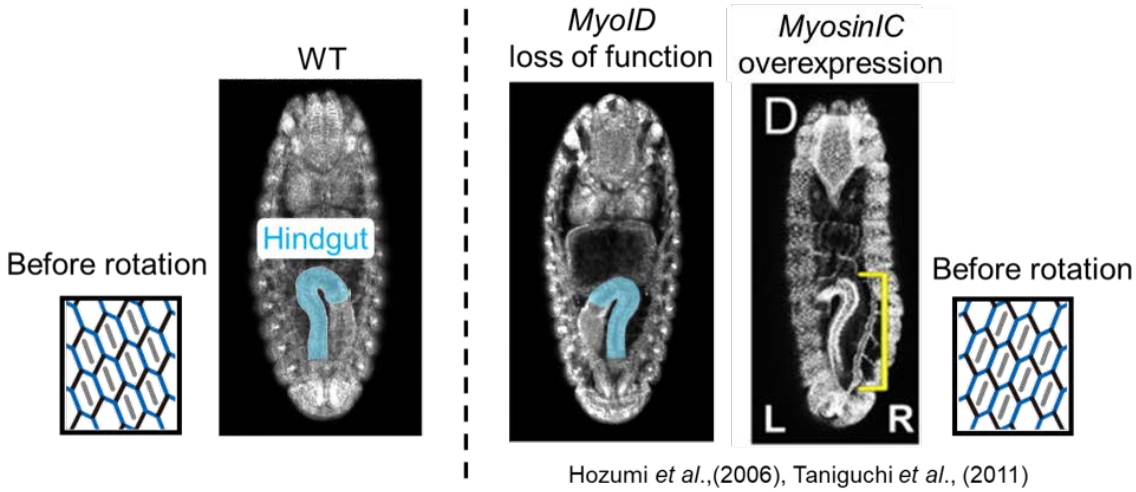

Figure 1: Schematic diagram of the relationship between type I myosin and embryonic hindgut in *Drosophila*. embryonic hindgut of wild type (WT) shows a constant left-right asymmetry. *Myo1D* loss of function or *Myo1C* overexpression reverses the left-right asymmetry.

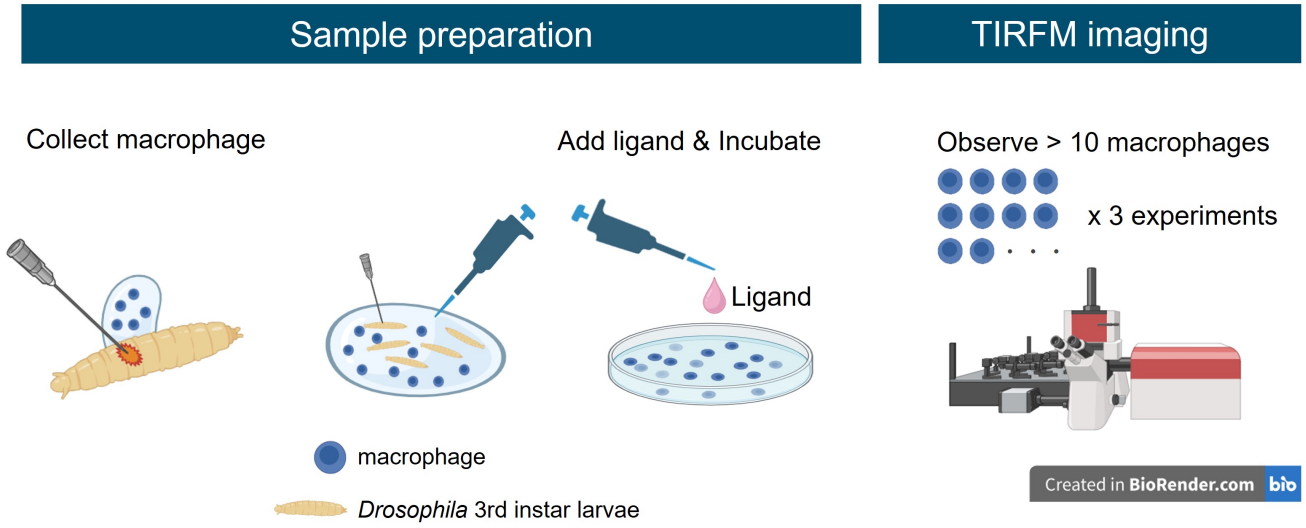

Figure 2: Schematic of single molecule imaging using macrophages collected from *Drosophila* larvae. Macrophages were collected by needle puncture on the larval body surface and labeled with HaloTag TMR ligand. They were then observed with TIRFM. At least 10 cells of macrophages were observed in each experiment, and this procedure was repeated three times for each protein.

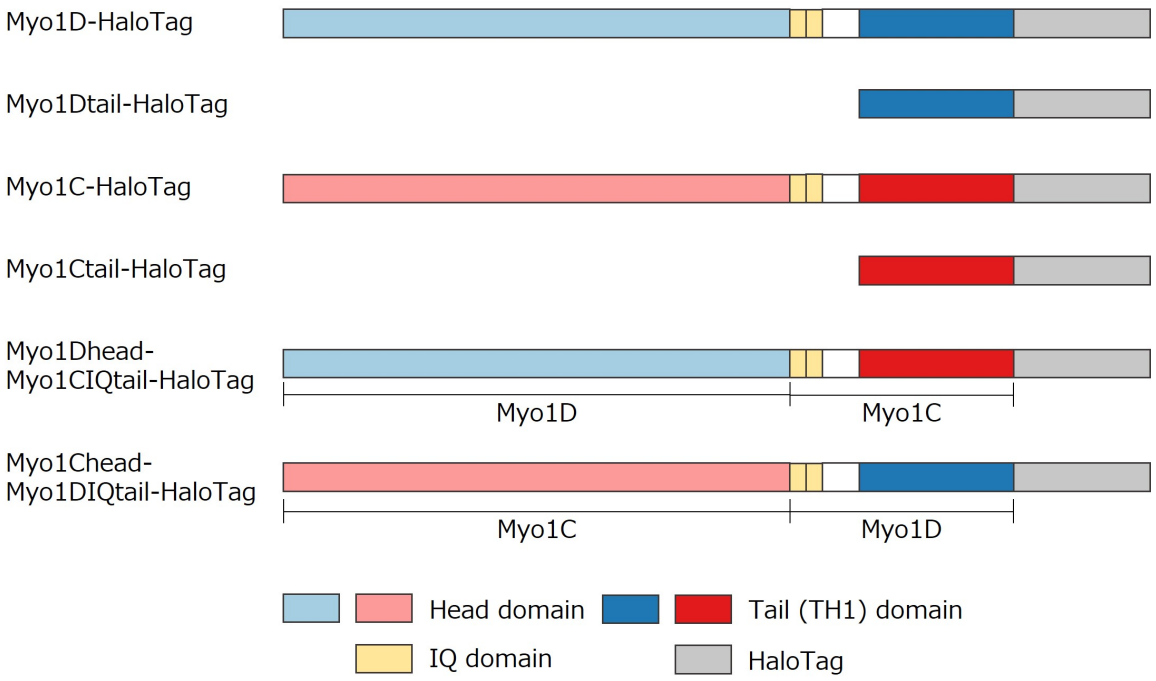

Figure 3: Schematic representations of Myo1D and Myo1C proteins and their respective derivatives analyzed in this study. The colored sections correspond to different domains of Myo1D and Myo1C, while the gray squares represent the fused HaloTag regions at the C-terminals.

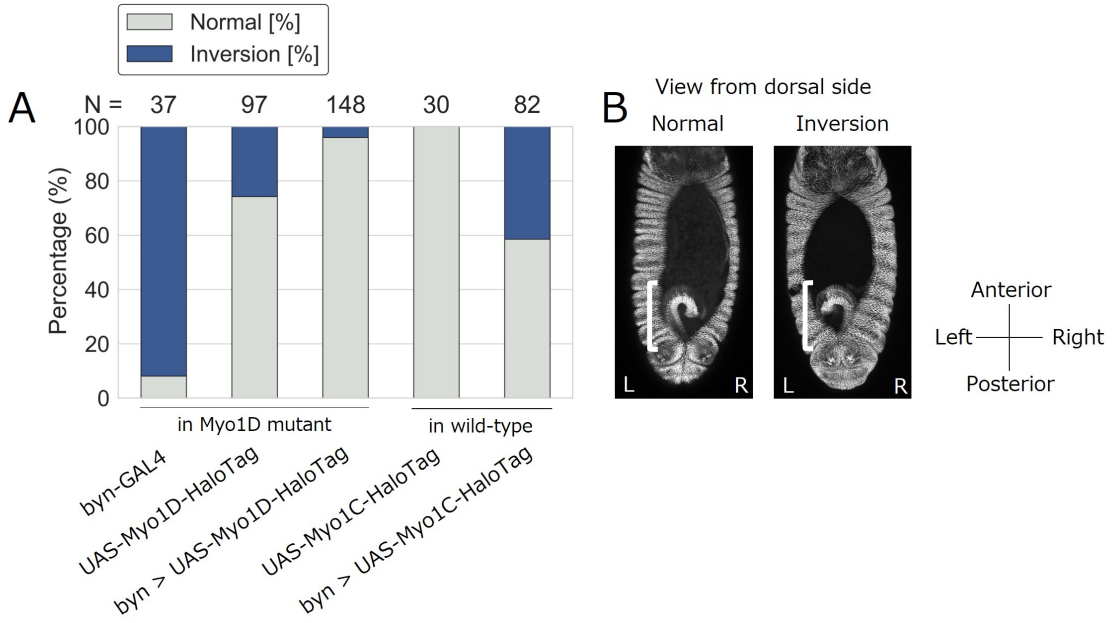

Figure 4: (A) Phenotypes of the hindgut in Myo1D mutant or wild-type embryos where hindgut-specific GAL4 driver, *byn-GAL* and/or UAS expressing Myo1D (UAS-Myo1D-HaloTag) or Myo1C (UAS-Myo1C-HaloTag). Percentages of normal (Normal) and inversed (Inversion) LR-asymmetry are shown in gray and blue, respectively. N indicates the number of embryos examined. (B) Representative examples of normal (Normal, wild type) and inversed (Inversion, $Myo1D^{L152}$ homozygote) LR asymmetry in the embryonic hindgut viewed from the ventral side. Embryos were stained with an anti-FasIII antibody. The hindgut is highlighted by white brackets. Left and right sides of embryos are indicated by L and R. Anterior is up.

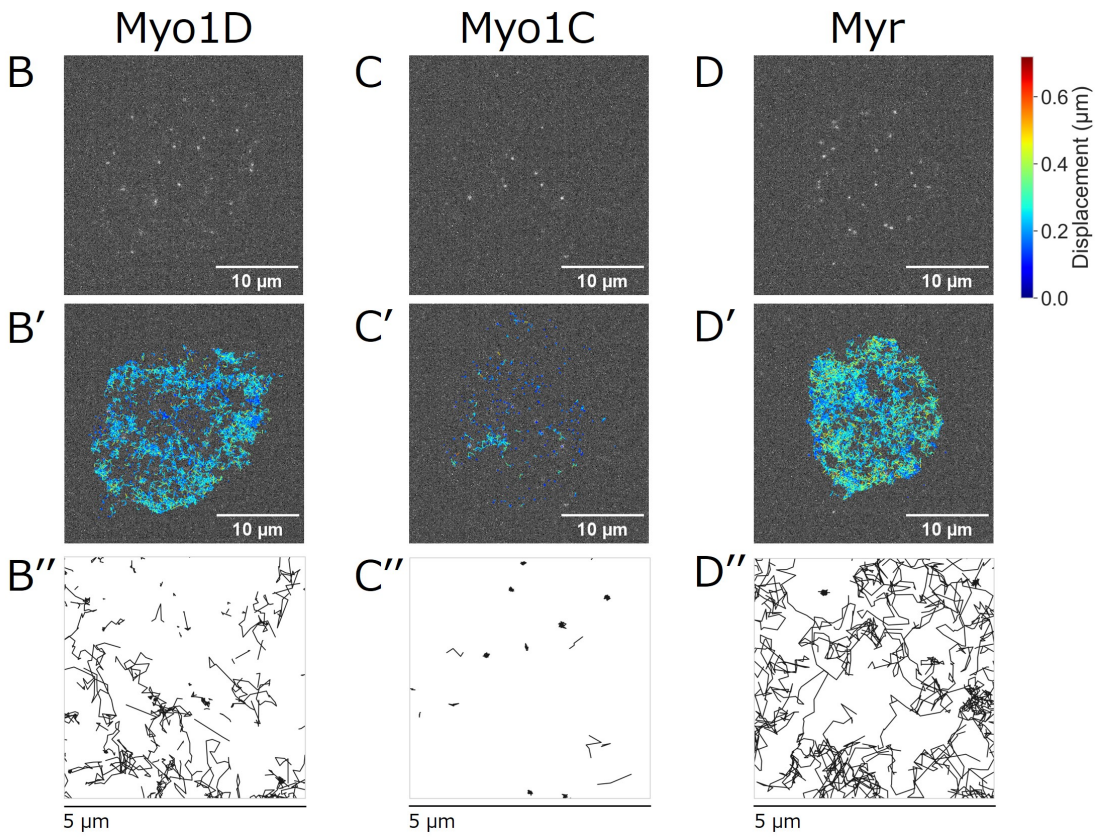

Figure 5: (A-C) Representative snapshots captured during single-molecule live imaging of Myo1D-HaloTag (A), Myo1C-HaloTag (B), and Myr-HaloTag (C) on the plasma membrane of *Drosophila* macrophages. (A'-C') Tracked trajectories of Myo1D-HaloTag (A'), Myo1C-HaloTag (B'), and Myr-HaloTag (C') for 20 s are shown in colored lines corresponding to the displacement distance (μm) as indicated in the right.

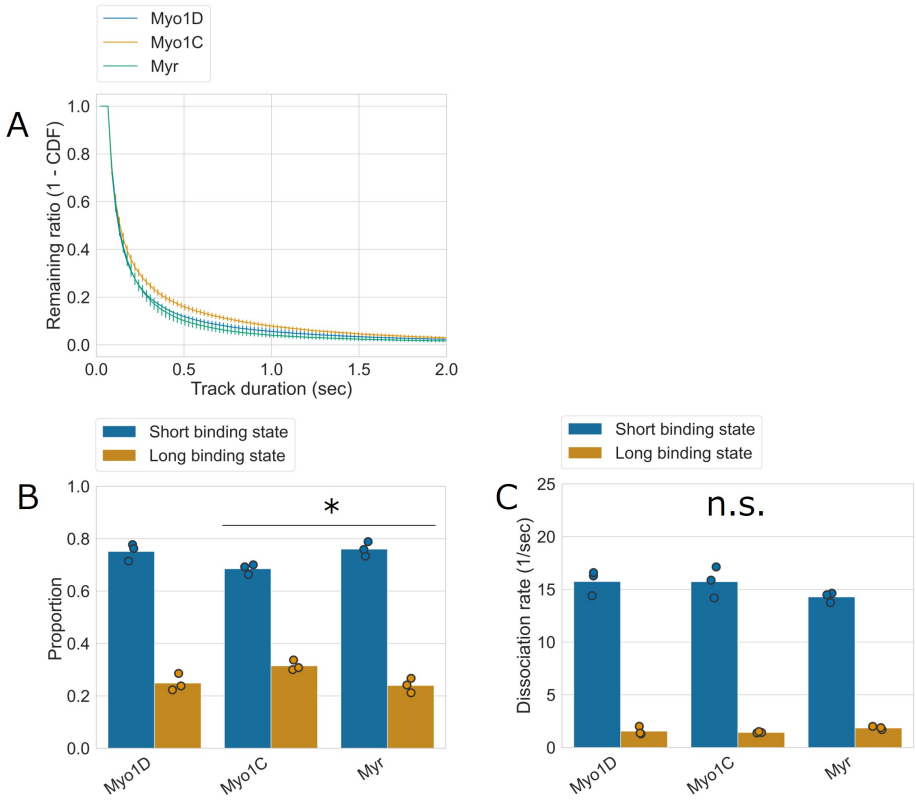

Figure 6: (A) Dissociation curve (mean ± s.d.) of Myo1D-HaloTag (Myo1D), Myo1C-HaloTag (Myo1C), and Myr-HaloTag (Myr) are shown in the indicated colors at the top. Remaining ratio is calculated as a complement cumulative distribution function (1 − CDF) of tracked durations. (B and C) Proportion (B) and dissociation rate (1/s) (C) of long (blue bars) and short (brown bars) binding states of Myo1D-HaloTag, Myo1C-HaloTag, and Myr-HaloTag. The bar indicates the mean value. P values were calculated by Tukey's all-pair comparison tests. The dots indicate values estimated from one

experiment. At least 10 cells were observed in one experiment. * and n.s. denote $p < 0.05$ and $p > 0.05$, respectively.

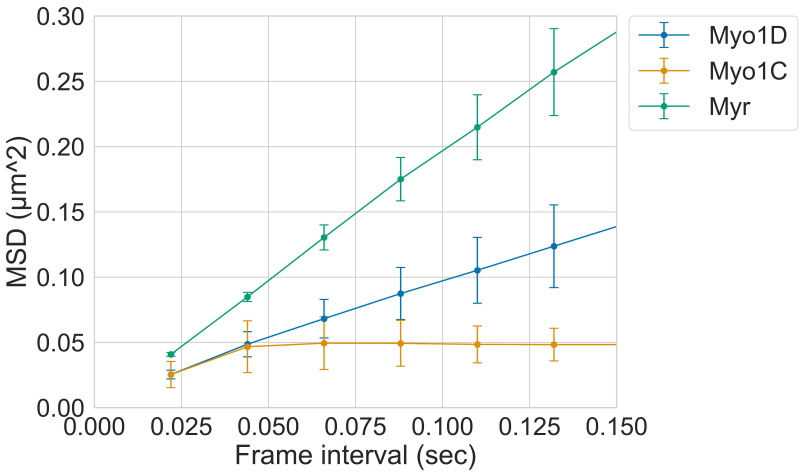

Figure 7: MSD (mean ± s.d.) of Myo1D-HaloTag, Myo1C-HaloTag, and Myr-HaloTag at various frame intervals (seconds) are shown.

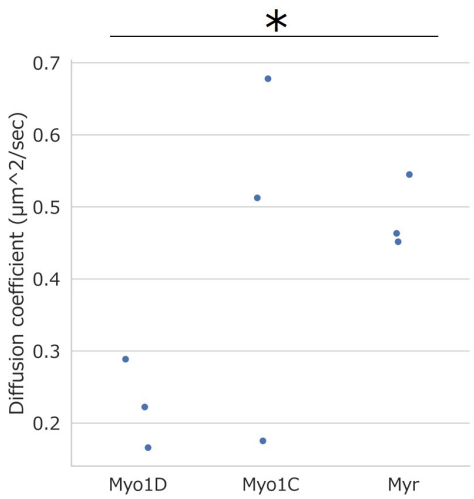

Figure 8: Diffusion coefficient (D_{MSD}) ($\mu m^2/s$) of Myo1D-HaloTag, Myo1C-HaloTag, and Myr-HaloTag estimated from MSD. The values of Myo1C is apparent values because Myo1C is undergo trapped diffusion. The dots indicate values estimated from one experiment, and at least 10 cells were observed in one experiment.

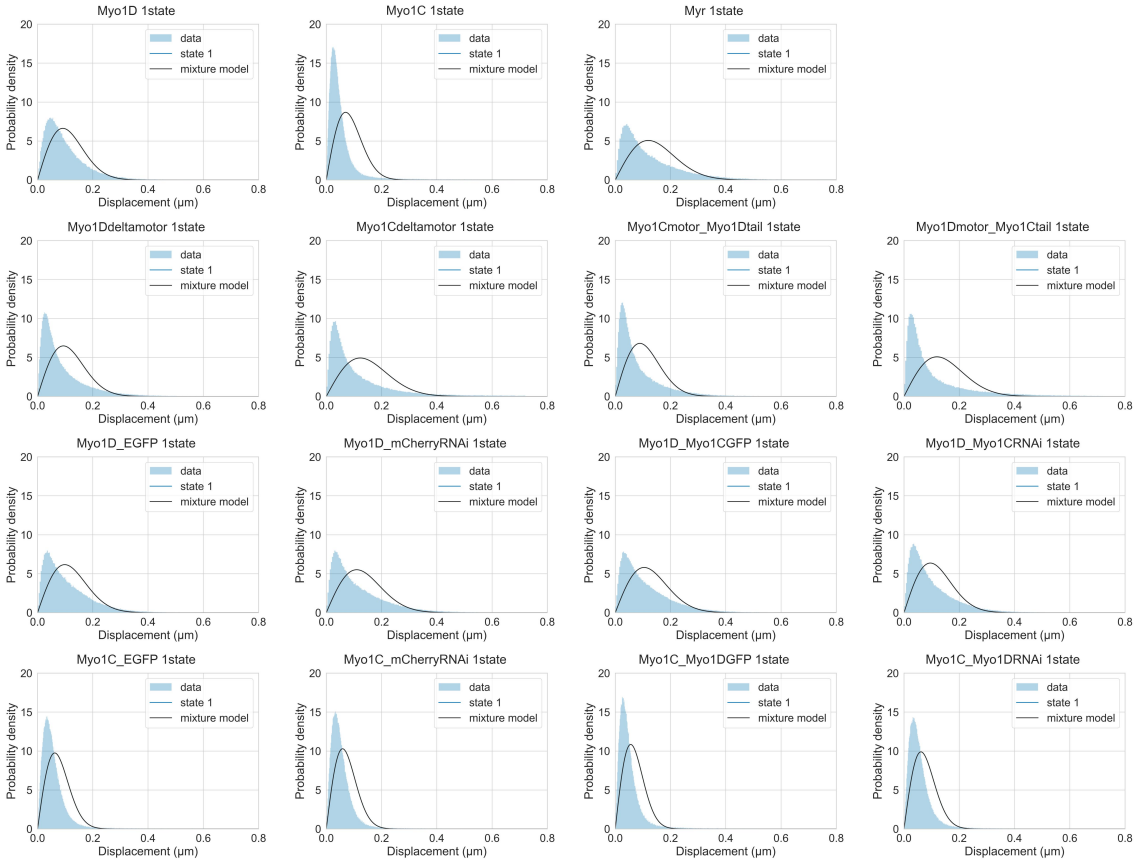

Figure 9: The probability density function obtained from the HMM assuming one state (black) is plotted against the histogram of the experimental data (blue). The distributions corresponding to each state are shown in the legend. Since this figure is a one-state HMM, the black and blue lines coincide.

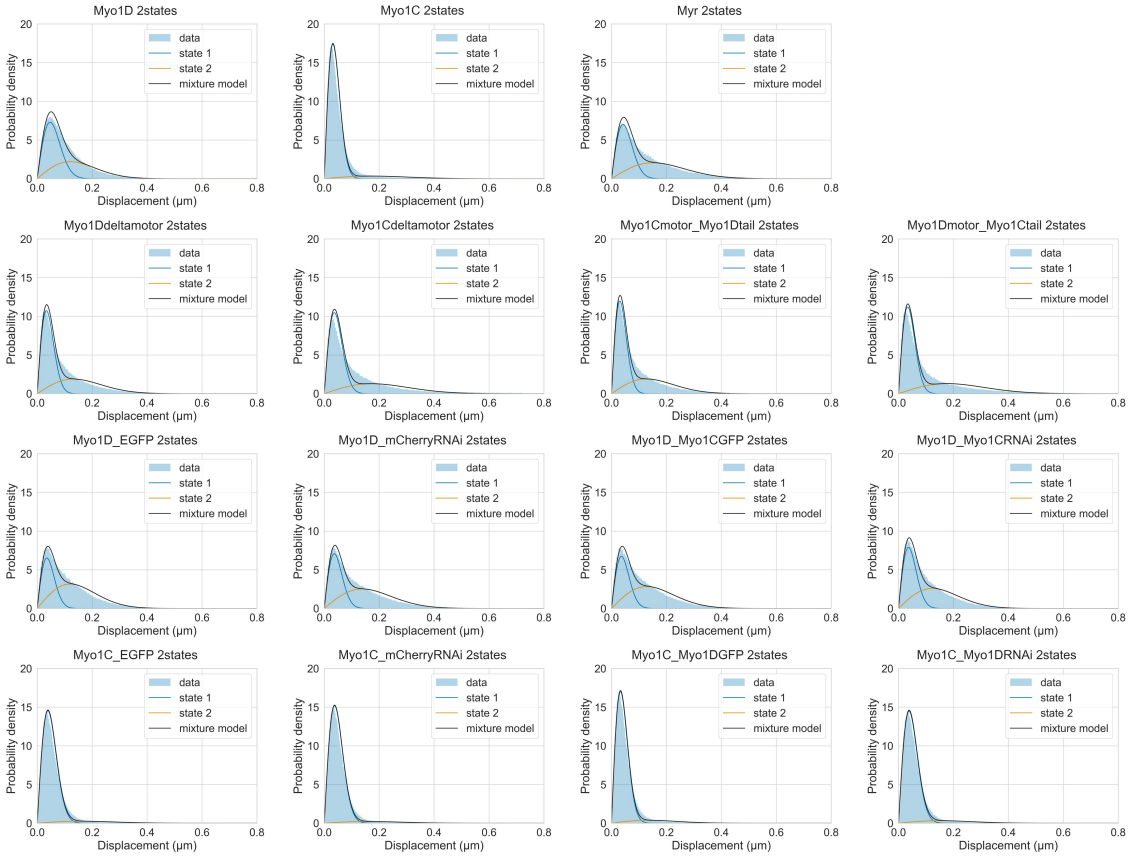

Figure 10: The probability density function obtained from the HMM assuming two state (black) is plotted against the histogram of the experimental data (blue). The distributions corresponding to each state are shown in the legend.

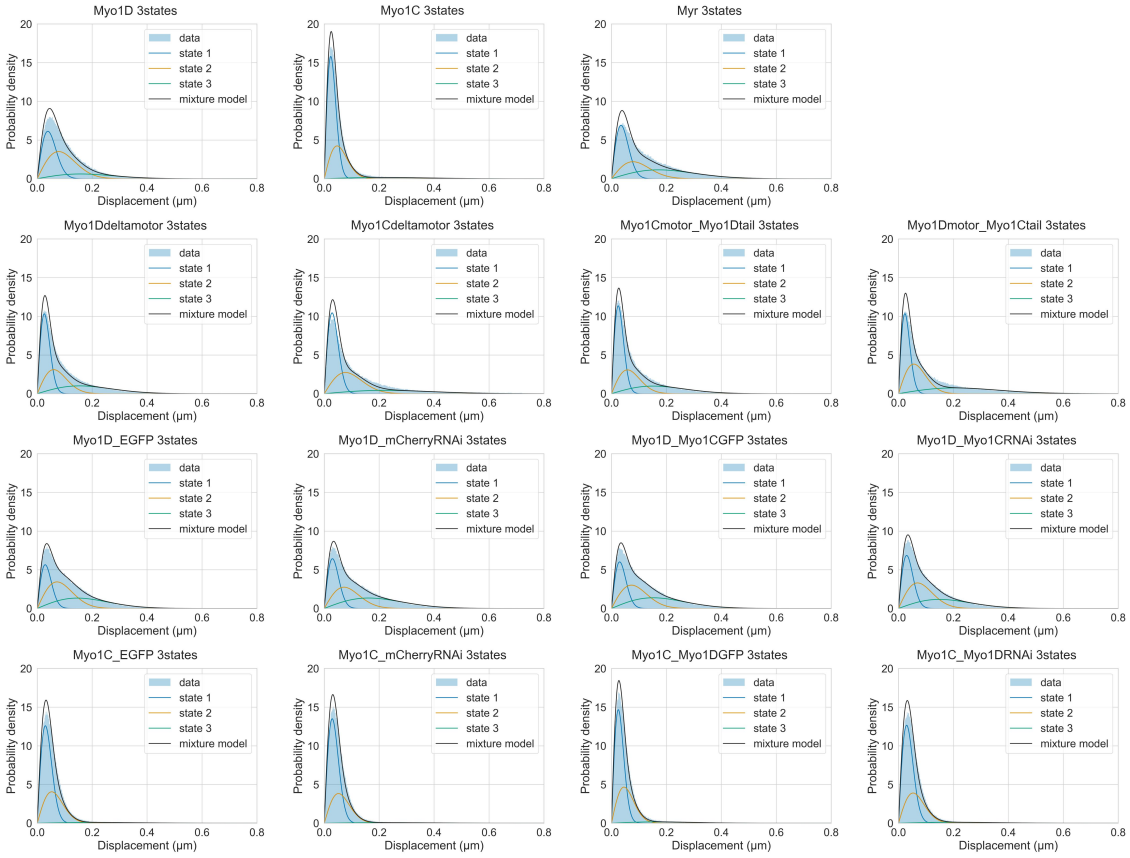

Figure 11: The probability density function obtained from the HMM assuming three state (black) is plotted against the histogram of the experimental data (blue). The distributions corresponding to each state are shown in the legend.

Figure 12: The trajectory of state assignment to the displacement series was visualized by the Viterbi algorithm based on the parameters estimated by the Baum-Welch algorithm.

Blue indicates slow diffusion states, brown indicates intermediate diffusion states, and green indicates fast diffusion states.

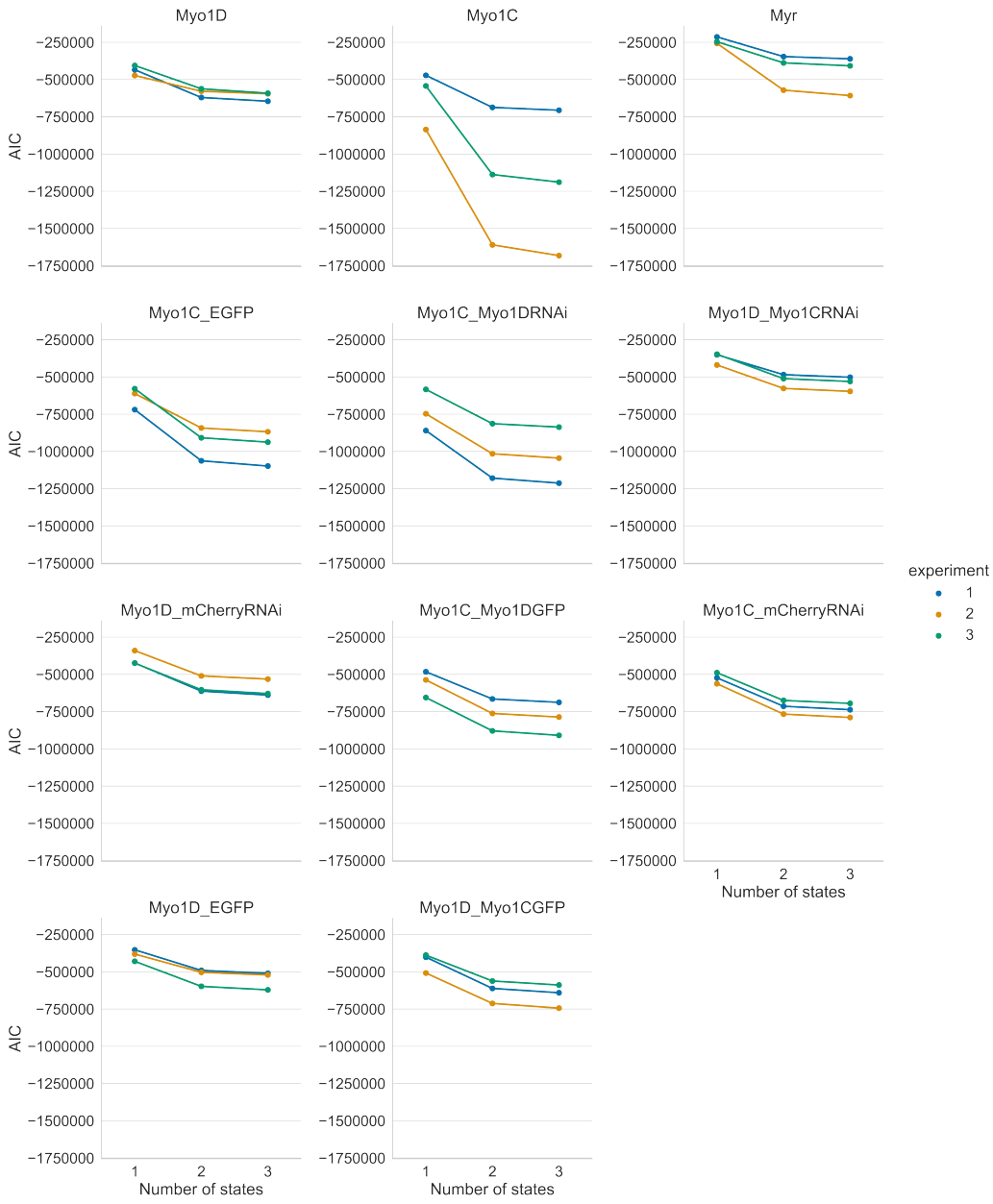
Myo1D
Myo1C
Myr
Myo1C_EGFP
Myo1C_Myo1DRNAi
Myo1D_Myo1CRNAi
Myo1D_mCherryRNAi
Myo1C_Myo1DGFP
Myo1C_mCherryRNAi
Myo1D_EGFP
Myo1D_Myo1CGFP
AIC
−250000
−500000
−750000
−1000000
−1250000
−1500000
−1750000
1
2
3
Number of states
experiment
1
2
3

Figure 13: The values of the AIC when the number of states is varied from one to three in the Baum-Welch algorithm. The color of the line indicates the value from identical experiment.

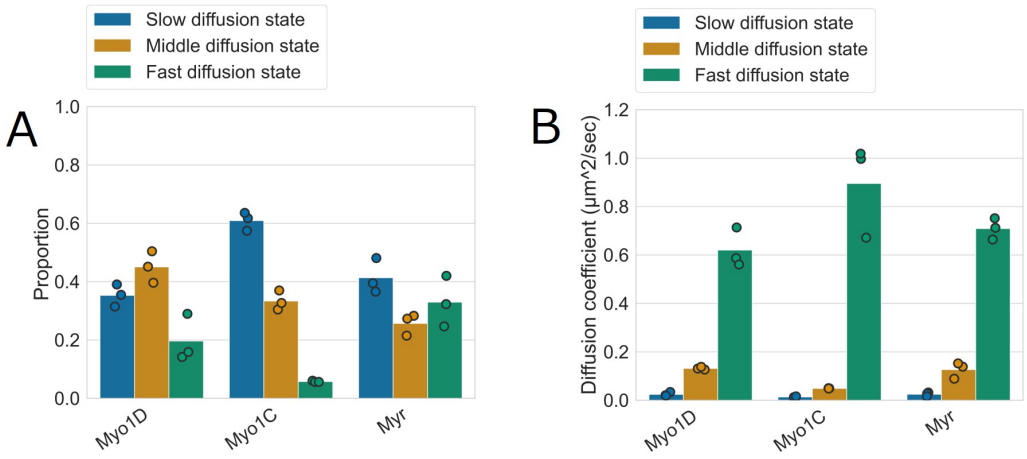

Figure 14: (A) Proportions of slow (blue bars), middle (brown bars), and fast (green bars) states estimated using the Baum-Welch algorithm. The bar indicates the mean value. The dots indicate values estimated from one experiment. At least 10 cells were observed in one experiment. (B) Diffusion coefficients (D_{HMM}) ($\mu m^2/s$) of slow (blue bars), middle (brown bars), and fast (green bars) diffusion states were estimated using the Baum-Welch algorithm. The bar indicates the mean value. The dots indicate values estimated from one experiment. At least 10 cells were observed in one experiment.

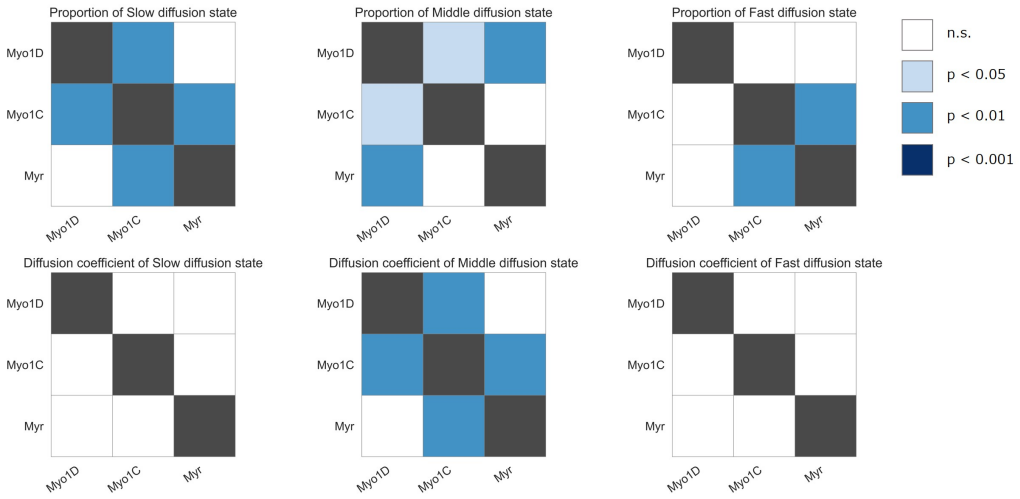

Figure 15: Table showing p values of Figure 14. P values are calculated by the Tukey's all-pairs comparison tests. n.s. ($p>0.05$), $p<0.05$, $p<0.01$, and $p<0.001$ are shown in respective colors, indicated in the right, in rectangles corresponding to paired comparison between the values stated at the top of each panel of Myo1D-HaloTag, Myo1C-HaloTag, and Myr-HaloTag. Comparison between itself are shown as NaN (Not a Number).

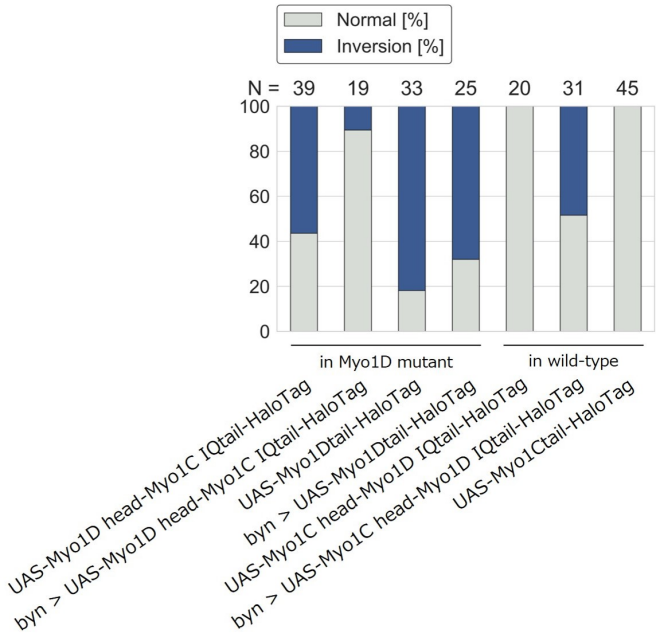

Figure 16: Phenotypes of the hindgut in Myo1D mutant or wild-type embryos where hindgut-specific GAL4 driver, *byn-GAL* and/or UAS construct express deletion and chimeric forms of Myo1D and Myo1C genes. Percentages of normal (Normal) and inversed (Inversion) LR-asymmetry are shown in gray and blue, respectively. N represents the number of embryos examined.

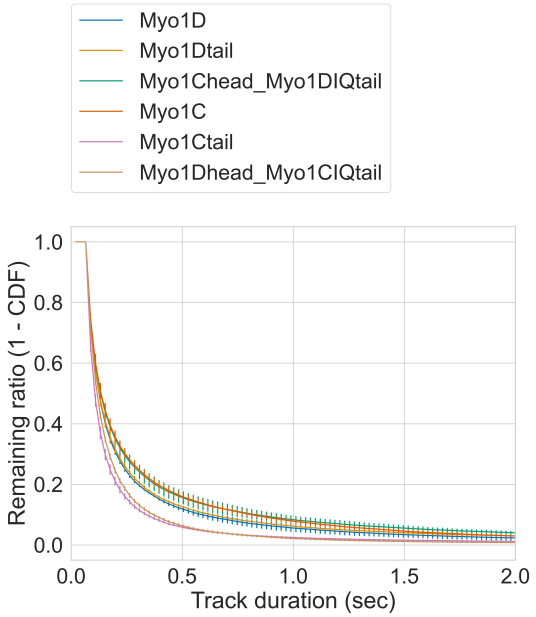

Figure 17: Dissociation curve (mean ± s.d.) of full-length myosins, head domain deleted myosins, and chimera myosins as indicated in the upper panel. Remaining ratio is calculated as a complement cumulative distribution function (1 − CDF) of tracked durations.

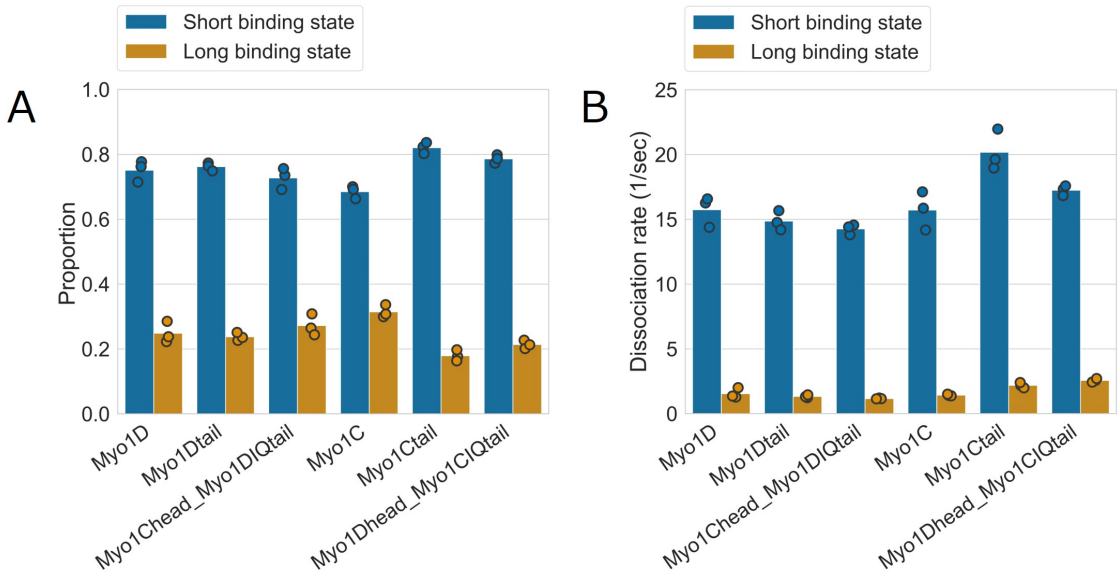

Figure 18: (A and B) Proportion (A) and dissociation rate (1/s) (B) of short (blue bars) and long (brown bars) binding states of deletion and chimeric Myo1D and Myo1C, as shown in Figure 3. The bar indicates the mean value.

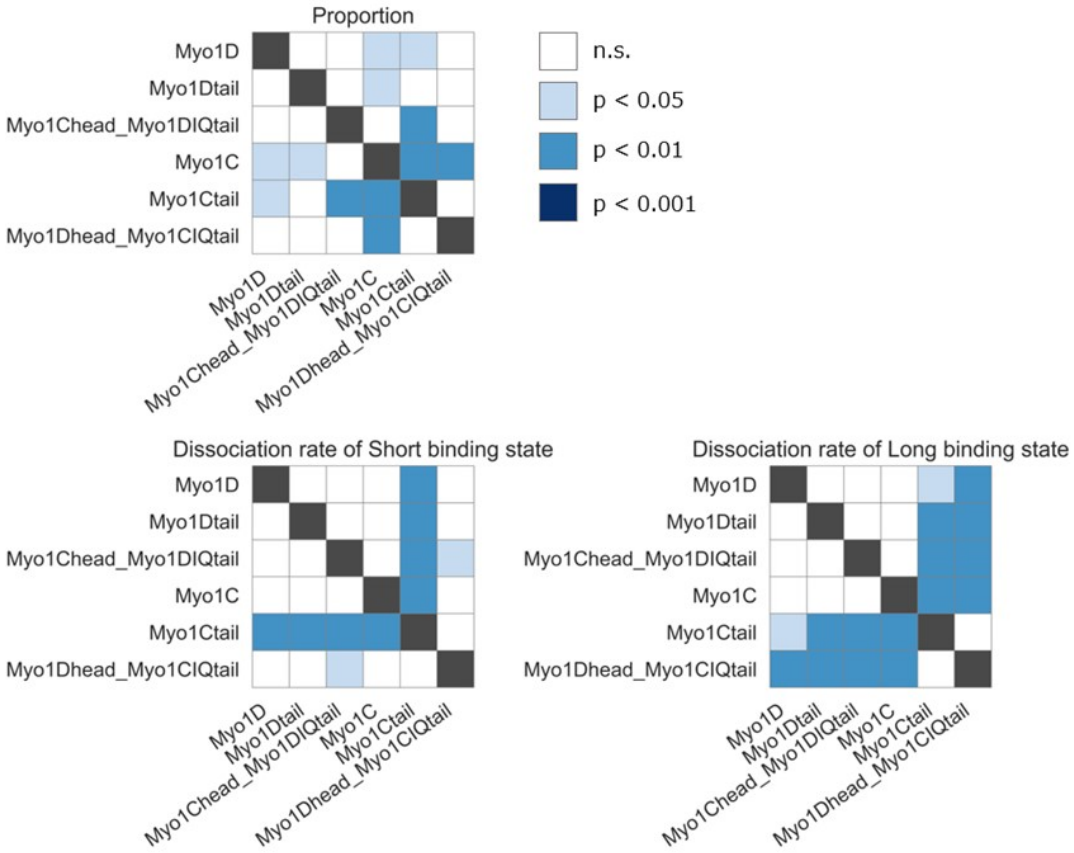

Figure 19: Tables displaying p values corresponding to binding states of Figure 18

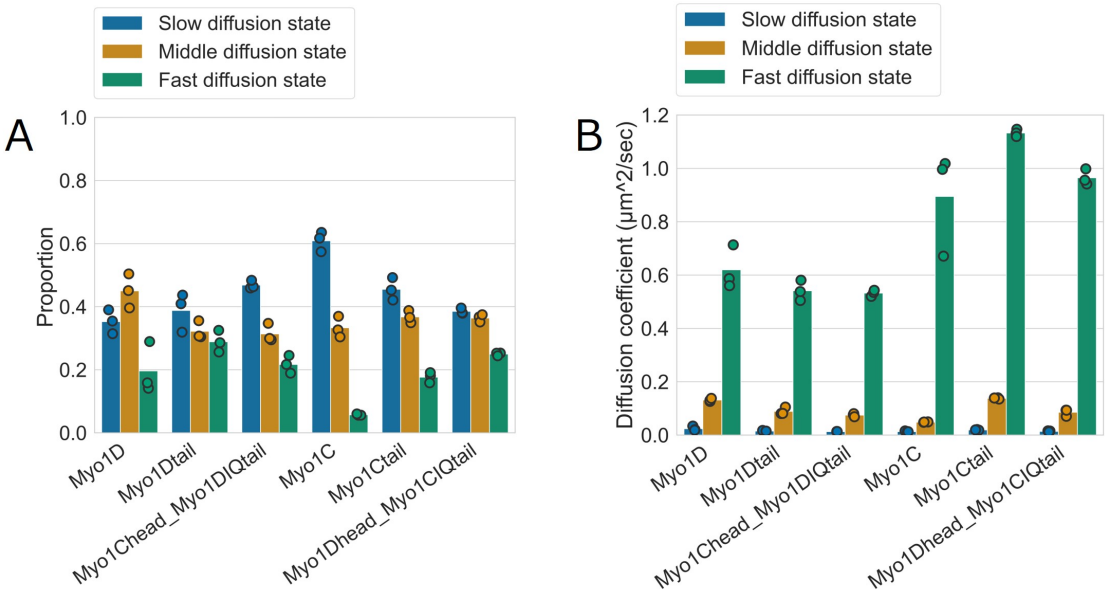

Figure 20: Proportion (A) and diffusion coefficients (D_{HMM}) ($\mu m^2/s$) (B) of slow (blue bars), middle (blown bars), and fast (green bars) diffusion states estimated using the Baum-Welch algorithm. The bar indicates the mean value.

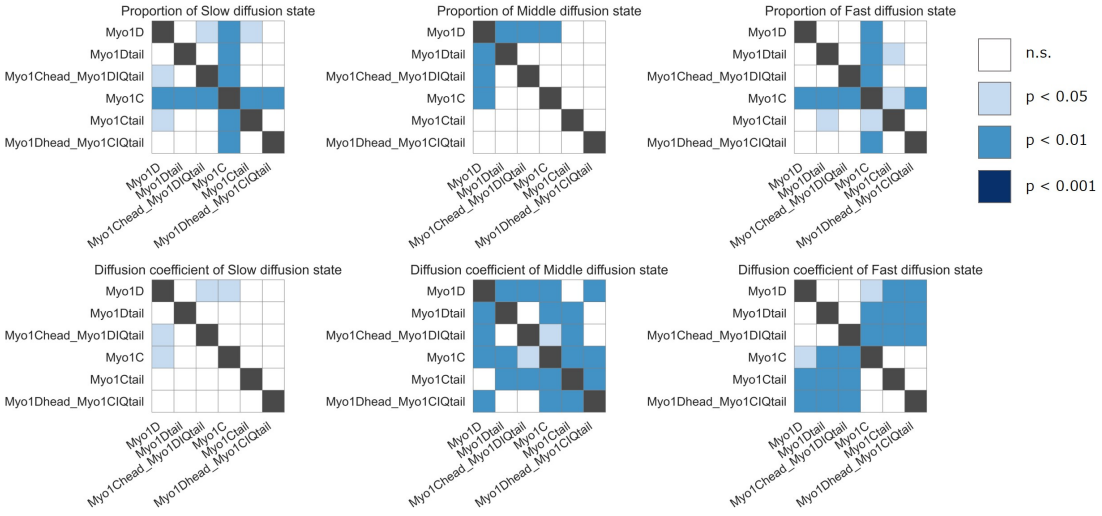

Figure 21: Tables displaying p values corresponding to binding states of Figure 20

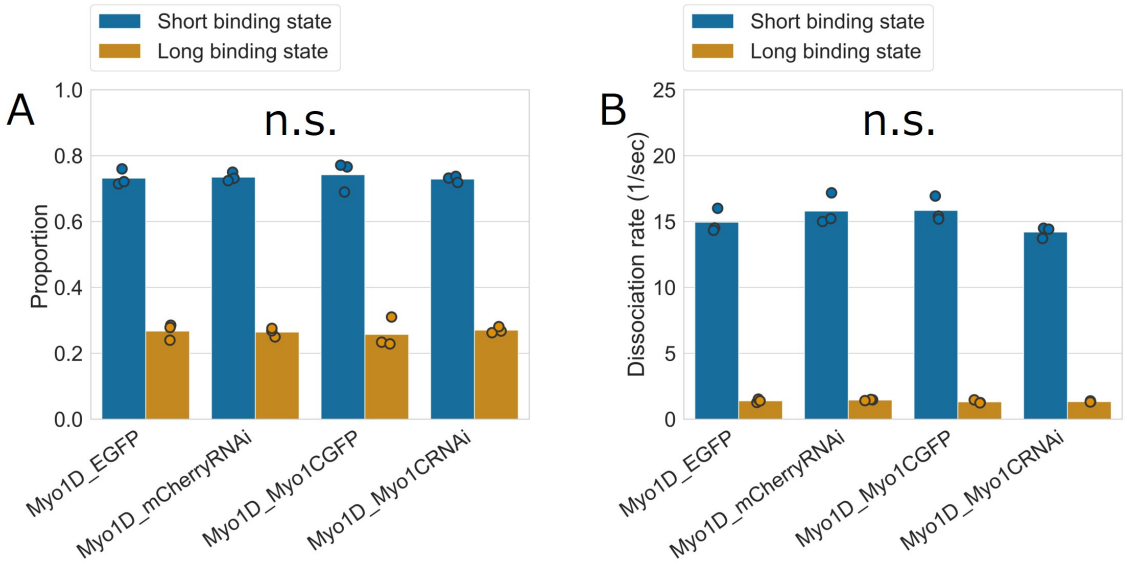

Figure 22: Proportion (A) and dissociation rate (1/s) (B) of short (blue bars) and long (brown bars) binding states of Myo1D-HaloTag (Myo1D) when misexpression or RNAi related to Myo1C were conducted as indicated at the bottom.

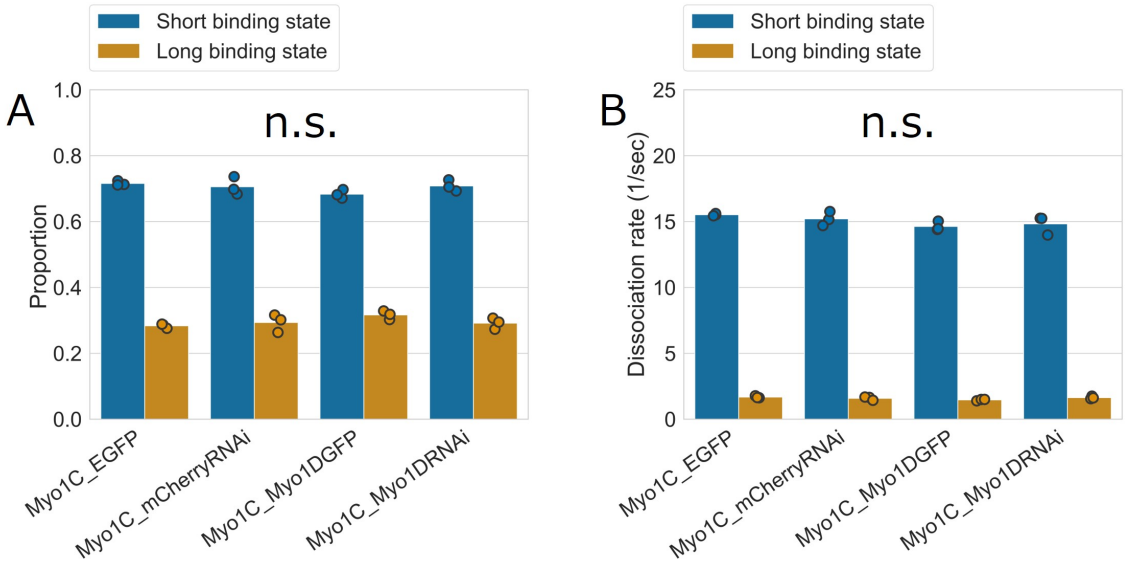

Figure 23: Proportion (A) and dissociation rate (1/s) (B) of short (blue bars) and long (brown bars) binding states of Myo1C-HaloTag (Myo1C) when misexpression or RNAi related to Myo1D were conducted as indicated at the bottom.

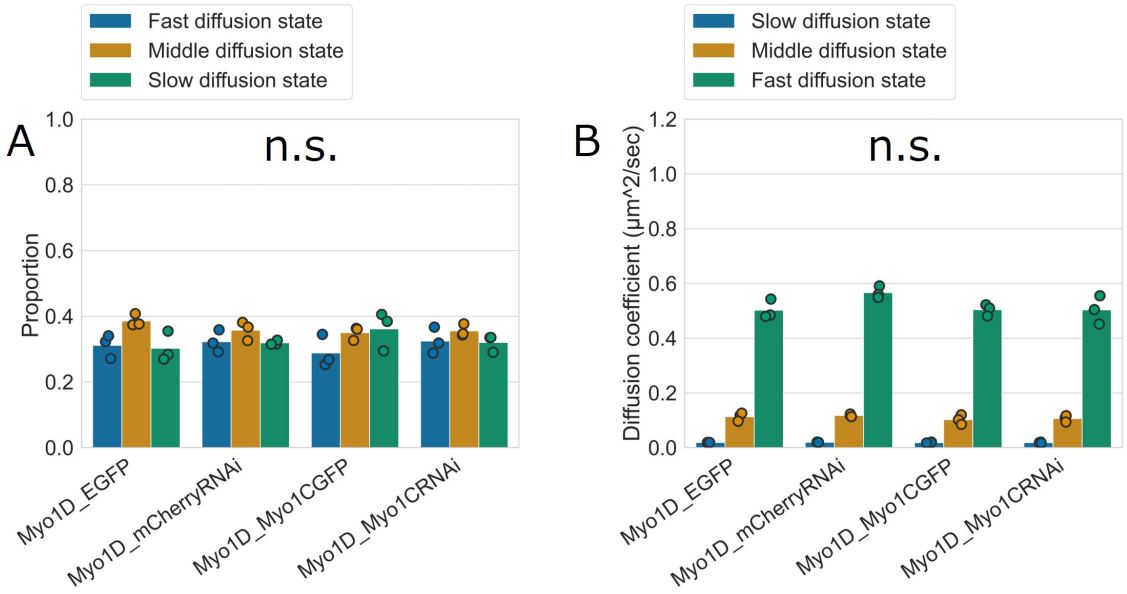

Figure 24: Proportion (A) and diffusion coefficients (D_{HMM}) ($\mu m^2/s$) (B) of slow (blue bars), middle (brown bars) and fast (green bars) diffusion states of Myo1D-HaloTag (Myo1D) when misexpression or RNAi related to Myo1C were conducted as indicated at the bottom.

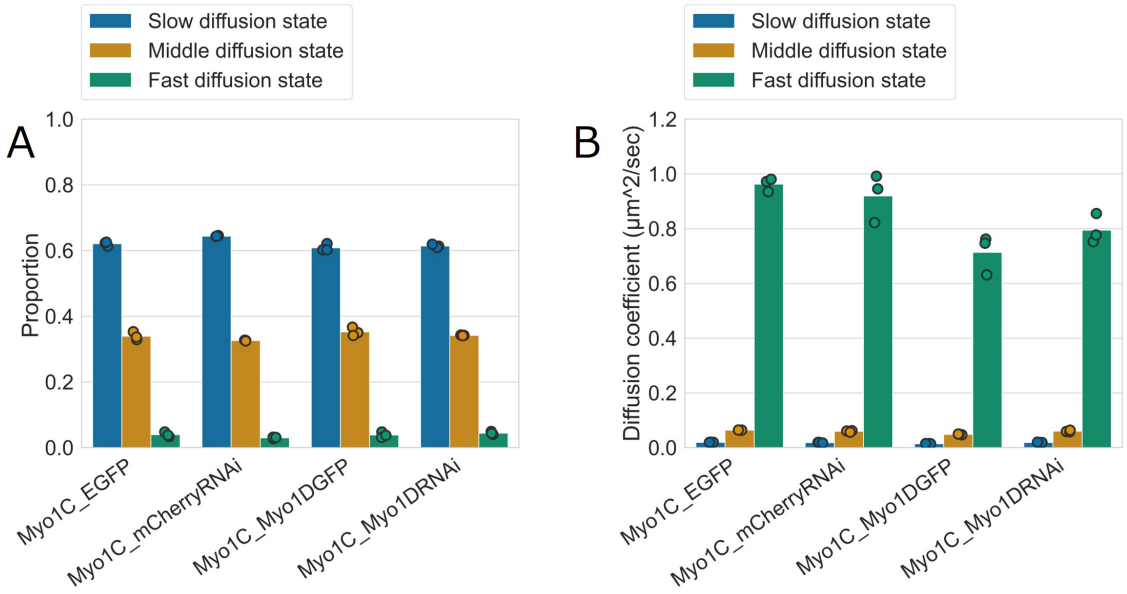

Figure 25: Proportion (A) and diffusion coefficients (D_{HMM}) (µm^2/s) (B) of slow (blue bars), middle (brown bars) and fast (green bars) diffusion states of Myo1C-HaloTag (Myo1C) when misexpression or RNAi related to Myo1D were conducted as indicated at the bottom.

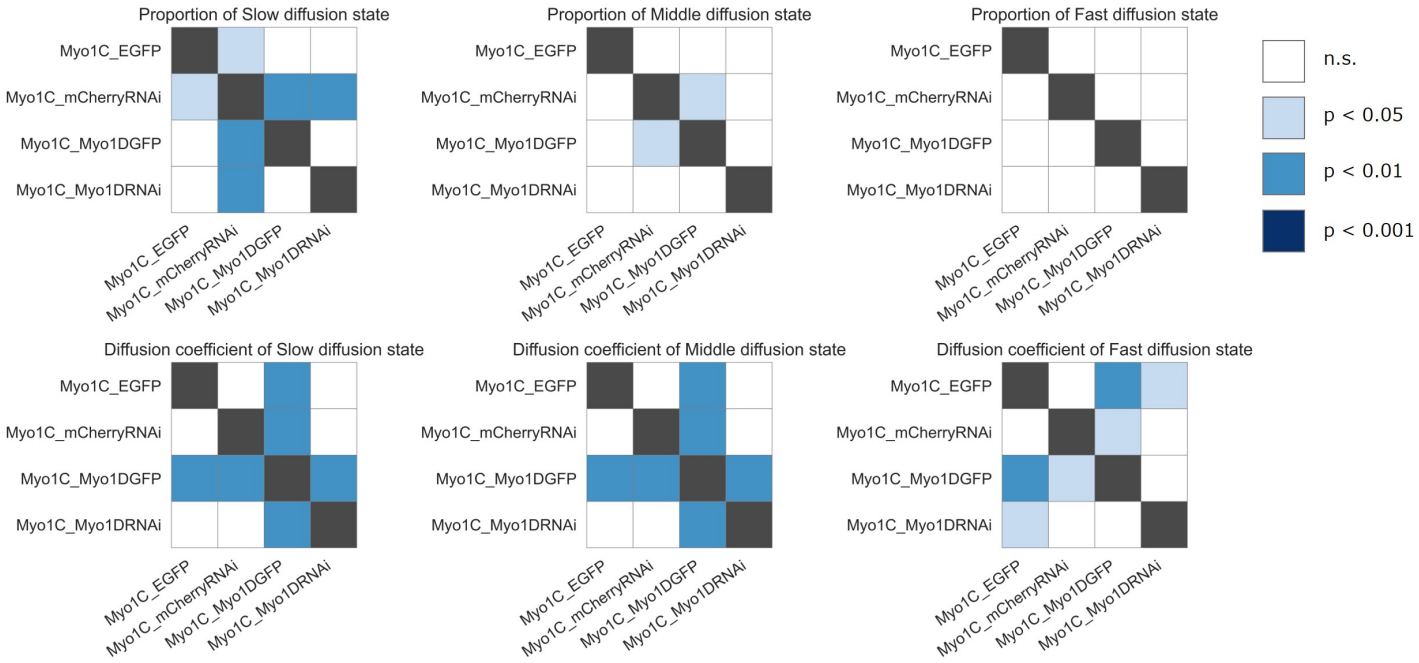

Figure 26: Tables showing p values of Figure 25. P values are calculated by Tukey's all-pairs comparison tests. n.s. ($p>0.05$), $p<0.05$, $p<0.01$, and $p<0.001$ are shown in respective colors, indicated in the right. Rectangles correspond to paired comparison between the values stated at the top of each panel. Comparison between itself are shown as NaN (Not a Number).

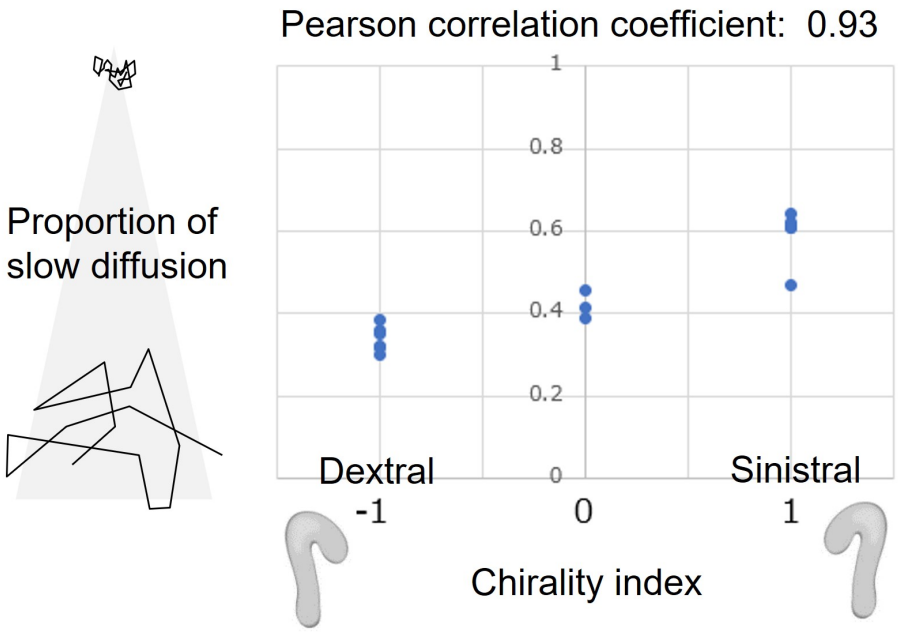

Figure 27: Correlation between chirality index and proportion of slow diffusion. x-axis is chirality index and y-axis is proportion of slow diffusion. Chirality index was set to -1 for dextral direction, 1 for sinistral direction, and 0 for no direction. For example, the chirality index of full-length Myo1D is -1, Myo1Dtail is 0, and full-length Myo1C is 1.

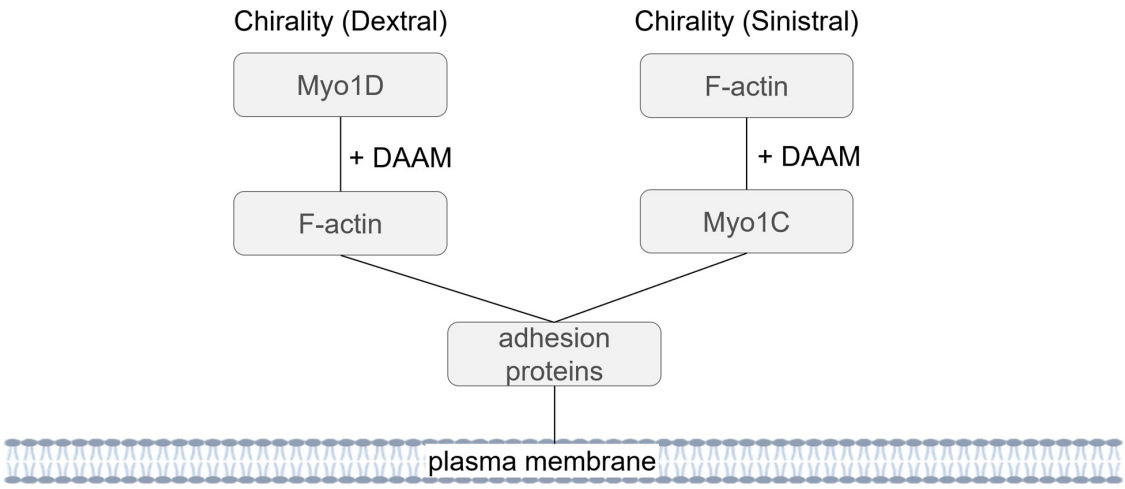

Figure 28: Hypothesis on *Drosophila* LR asymmetry and the connection between myosins. Myo1D and DAAM imparts chirality to F-actin, which is then transmitted to the plasma membrane and cytoskeleton via adhesion proteins. Myo1C transfers the DAAM-dependent F-actin chirality to the plasma membrane and cytoskeleton via adhesion proteins.

6. Table

Table 1: Diffusion coefficient (D_{MSD}) ($\mu m^2/s$) obtained by fitting the MSD function specified in MSD model column (Brownian motion: Equation 3, Confined diffusion: Equation 4). The values are mean ± s.d.

Protein	Apparent D_{MSD} ($\mu m^2/s$) ± s.d.	MSD model
Myo1C	0.46 ± 0.26	Confined diffusion
Myo1C_EGFP	0.29 ± 0.09	Confined diffusion
Myo1C_Myo1DGFP	0.24 ± 0.02	Confined diffusion
Myo1C_Myo1DRNAi	0.13 ± 0.07	Confined diffusion
Myo1C_mCherryRNAi	0.17 ± 0.01	Confined diffusion
Myo1Chead_Myo1DIQtail	0.22 ± 0.02	Brownian motion
Myo1Ctail	0.35 ± 0.01	Brownian motion
Myo1D	0.23 ± 0.06	Brownian motion
Myo1D_EGFP	0.29 ± 0.04	Brownian motion
Myo1D_Myo1CGFP	0.26 ± 0.06	Brownian motion
Myo1D_Myo1CRNAi	0.27 ± 0.02	Brownian motion
Myo1D_mCherryRNAi	0.32 ± 0.03	Brownian motion
Myo1Dhead_Myo1CIQtail	0.38 ± 0.02	Brownian motion
Myo1Dtail	0.29 ± 0.06	Brownian motion
Myr	0.49 ± 0.05	Brownian motion

Table 2: Proportion and dissociation rate (1/s) obtained by fitting weighted sum of exponential functions. The values are mean ± s.d.

Protein	State	Proportion ± s.d.	Dissociation rate (1/s) ± s.d.
Myo1C	Long binding state	0.31 ± 0.02	1.43 ± 0.06
	Short binding state	0.69 ± 0.02	15.72 ± 1.48
Myo1C_EGFP	Long binding state	0.28 ± 0.01	1.68 ± 0.08
	Short binding state	0.72 ± 0.01	15.53 ± 0.09
Myo1C_Myo1DGFP	Long binding state	0.32 ± 0.01	1.47 ± 0.06
	Short binding state	0.68 ± 0.01	14.64 ± 0.35
Myo1C_Myo1DRNAi	Long binding state	0.29 ± 0.02	1.64 ± 0.10
	Short binding state	0.71 ± 0.02	14.83 ± 0.73
Myo1C_mCherryRNAi	Long binding state	0.29 ± 0.03	1.59 ± 0.13
	Short binding state	0.71 ± 0.03	15.21 ± 0.54
Myo1Chead_Myo1DIQtail	Long binding state	0.27 ± 0.03	1.17 ± 0.03
	Short binding state	0.73 ± 0.03	14.26 ± 0.40
Myo1Ctail	Long binding state	0.18 ± 0.02	2.19 ± 0.20
	Short binding state	0.82 ± 0.02	20.19 ± 1.58
Myo1D	Long binding state	0.25 ± 0.03	1.55 ± 0.40
	Short binding state	0.75 ± 0.03	15.75 ± 1.19
Myo1D_EGFP	Long binding state	0.27 ± 0.02	1.40 ± 0.13
	Short binding state	0.73 ± 0.02	14.96 ± 0.92
Myo1D_Myo1CGFP	Long binding state	0.26 ± 0.05	1.32 ± 0.13
	Short binding state	0.74 ± 0.05	15.85 ± 0.95
Myo1D_Myo1CRNAi	Long binding state	0.27 ± 0.01	1.34 ± 0.04
	Short binding state	0.73 ± 0.01	14.21 ± 0.43
Myo1D_mCherryRNAi	Long binding state	0.26 ± 0.01	1.46 ± 0.04

	Short binding state	0.74 ± 0.01	15.81 ± 1.20
Myo1Dhead_Myo1CIQtail	Long binding state	0.21 ± 0.01	2.58 ± 0.14
	Short binding state	0.79 ± 0.01	17.25 ± 0.38
Myo1Dtail	Long binding state	0.24 ± 0.01	1.34 ± 0.11
	Short binding state	0.76 ± 0.01	14.88 ± 0.75
Myr	Long binding state	0.24 ± 0.03	1.85 ± 0.15
	Short binding state	0.76 ± 0.03	14.28 ± 0.48

Table 3: AIC values of all genes obtained by Baum-Welch algorithms. The values are mean of three experiments.

Protein	Number of states	AIC
Myo1C	1	-616642.0983
	2	-1144859.592
	3	-1192357.31
Myo1C_EGFP	1	-636398.9342
	2	-937955.6255
	3	-967982.7736
Myo1C_Myo1DGFP	1	-558352.329
	2	-768981.2737
	3	-794582.9084
Myo1C_Myo1DRNAi	1	-730044.6869
	2	-1002784.756
	3	-1031587.617
Myo1C_mCherryRNAi	1	-524821.626
	2	-718653.9702
	3	-740458.1555
Myo1Chead_Myo1DIQtail	1	-427488.4954
	2	-742241.4236
	3	-781490.8983
Myo1Ctail	1	-238971.4001
	2	-551256.0065
	3	-602838.0076
Myo1D	1	-437679.6636
	2	-587041.8432

	3	-611019.5818
Myo1D_EGFP	1	-387726.9395
	2	-530689.1257
	3	-550985.4883
Myo1D_Myo1CGFP	1	-432730.3451
	2	-628664.9224
	3	-657840.6293
Myo1D_Myo1CRNAi	1	-372605.3236
	2	-524218.3055
	3	-543064.8338
Myo1D_mCherryRNAi	1	-396254.5406
	2	-575317.4433
	3	-599976.9792
Myo1Dhead_Myo1CIQtail	1	-236610.466
	2	-532732.4456
	3	-566352.9848
Myo1Dtail	1	-538074.3227
	2	-887926.629
	3	-944490.4126
Myr	1	-238897.8449
	2	-434970.6207
	3	-458895.4299

Table 4: Proportion and diffusion coefficient (D_{HMM}) ($\mu m^2/s$) obtained by Baum-Welch algorithm. The values are mean ± s.d.

Protein	**State**	**Proportion ± s.d.**	**Apparent D_{HMM} ($\mu m^2/s$) ± s.d.**
Myo1C	Slow diffusion state	0.61 ± 0.03	0.01 ± 0.00
	Middle diffusion state	0.33 ± 0.03	0.05 ± 0.00
	Fast diffusion state	0.06 ± 0.00	0.90 ± 0.19
Myo1C_EGFP	Slow diffusion state	0.62 ± 0.01	0.02 ± 0.00
	Middle diffusion state	0.34 ± 0.01	0.06 ± 0.00
	Fast diffusion state	0.04 ± 0.01	0.96 ± 0.02
Myo1C_mCherryRNAi	Slow diffusion state	0.64 ± 0.00	0.02 ± 0.00
	Middle diffusion state	0.33 ± 0.00	0.06 ± 0.00
	Fast diffusion state	0.03 ± 0.00	0.92 ± 0.09
Myo1C_Myo1DGFP	Slow diffusion state	0.61 ± 0.01	0.01 ± 0.00
	Middle diffusion state	0.35 ± 0.01	0.05 ± 0.00
	Fast diffusion state	0.04 ± 0.01	0.71 ± 0.07
Myo1C_Myo1DRNAi	Slow diffusion state	0.61 ± 0.00	0.02 ± 0.00
	Middle diffusion state	0.34 ± 0.00	0.06 ± 0.00
	Fast diffusion state	0.04 ± 0.00	0.79 ± 0.05
Myo1Chead_Myo1DIQtail	Slow diffusion state	0.47 ± 0.01	0.01 ± 0.00
	Middle diffusion state	0.31 ± 0.03	0.08 ± 0.01

	Fast diffusion state	0.22 ± 0.03	0.53 ± 0.01
Myo1Ctail	Slow diffusion state	0.46 ± 0.04	0.02 ± 0.00
	Middle diffusion state	0.37 ± 0.02	0.14 ± 0.00
	Fast diffusion state	0.18 ± 0.02	1.13 ± 0.01
Myo1D	Slow diffusion state	0.35 ± 0.04	0.02 ± 0.01
	Middle diffusion state	0.45 ± 0.05	0.13 ± 0.01
	Fast diffusion state	0.20 ± 0.08	0.62 ± 0.08
Myo1D_EGFP	Slow diffusion state	0.30 ± 0.05	0.02 ± 0.00
	Middle diffusion state	0.39 ± 0.02	0.11 ± 0.02
	Fast diffusion state	0.31 ± 0.04	0.50 ± 0.04
Myo1D_mCherryRNAi	Slow diffusion state	0.32 ± 0.01	0.02 ± 0.00
	Middle diffusion state	0.36 ± 0.03	0.12 ± 0.00
	Fast diffusion state	0.32 ± 0.03	0.57 ± 0.02
Myo1D_Myo1CGFP	Slow diffusion state	0.36 ± 0.06	0.02 ± 0.00
	Middle diffusion state	0.35 ± 0.02	0.10 ± 0.02
	Fast diffusion state	0.29 ± 0.05	0.50 ± 0.02
Myo1D_Myo1CRNAi	Slow diffusion state	0.32 ± 0.03	0.02 ± 0.00
	Middle diffusion state	0.36 ± 0.02	0.11 ± 0.01
	Fast diffusion state	0.32 ± 0.04	0.50 ± 0.05
Myo1Dhead_Myo1CIQtail	Slow diffusion state	0.39 ± 0.01	0.01 ± 0.00
	Middle diffusion state	0.36 ± 0.01	0.09 ± 0.01

	Fast diffusion state	0.25 ± 0.00	0.97 ± 0.03
Myo1Dtail	Slow diffusion state	0.39 ± 0.06	0.02 ± 0.00
	Middle diffusion state	0.32 ± 0.03	0.09 ± 0.01
	Fast diffusion state	0.29 ± 0.03	0.54 ± 0.04
Myr	Slow diffusion state	0.41 ± 0.06	0.02 ± 0.01
	Middle diffusion state	0.26 ± 0.04	0.13 ± 0.03
	Fast diffusion state	0.33 ± 0.09	0.71 ± 0.04

7. Experiment procedures

7.1 Generation of plasmids and transgenic lines

Idesigned and generated the following constructs: UAS-Myo1D-HaloTag, UAS-Myo1C-HaloTag, UAS-Myo1Dtail-HaloTag, UAS-Myo1Ctail-HaloTag, UAS-Myo1Dhead-Myo1CIQtail-HaloTag, and UAS-Myo1Chead-Myo1DIQtail-HaloTag. I followed established definitions of the amino acid sequences of the motor domain, IQ domain, and tail domains of Myo1D and Myo1C, as previously described (Hozumi et al., 2008; Morgan et al., 1994). Iisolated full-length Myo1D and Myo1C cDNAs by PCR amplification using cDNA obtained from *Drosophila* Gold Collection SD01662 (DGRC Stock Number: 5476) and GEO03137 (DGRC Stock Number: 1659954), respectively. Additional myosin cDNAs were sourced from previously generated plasmids (Hozumi et al., 2008). HaloTag sequences were derived from pFC15K (Promega). An EcoRI site was introduced at the N-terminus of the myosin PCR fragments, while a HaloTag-overlapping region was added at the C-terminus to facilitate the Seamless Ligation Cloning Extract (SLiCE) reaction (Motohashi, 2015). For the fragment encoding HaloTag, sequences that overlapped with myosin genes and specific restriction sites (KpnI site for UAS-Myo1D-HaloTag and EcoRI for the rest) were appended to the 5′ and 3′ ends, respectively. The myosin fragments and HaloTag fragments were then cloned into linearized pUAStattB via the SLiCE reaction. To generate transgenic lines, the resulting constructs were integrated into the *68A4*

P{CaryP}attP2 site of the third chromosome using the PhiC31/attP/attB system (Bateman, Lee, & Wu, 2006).

7.2 *Drosophila* strains

Drosophila lines were cultured and bred in vials containing a standard medium at 25°C. For Myo1D null alleles, I used $Myo1D^{L152}$ and $Myo1D^{K2}$ strains (Hozumi et al., 2006; Spéder et al., 2006). The following GAL4 lines were used in this study: *byn-GAL4* (Iwaki & Lengyel, 2002) and *He-GAL4* (Bloomington #8699). These GAL4 drivers specifically target the hindgut and macrophages, respectively (Iwaki & Lengyel, 2002; Zettervall et al., 2004). The following UAS lines were used in this study: UAS-myr-HaloTag (Bloomington #58396), UAS-Myo1D-HaloTag, UAS-Myo1D tail-HaloTag, UAS-Myo1C-HaloTag, UAS-Myo1C tail-HaloTag, UAS-Myo1D head-Myo1C IQ tail-HaloTag, UAS-Myo1C head-Myo1D IQ tail-HaloTag, UAS-Myo1D-GFP (Spéder et al., 2006), UAS-Myo1D-RNAi (Bloomington #33971), UAS-Myo1C-RNAi (Bloomington #41689), UAS-EGFP (Kyoto DGRC #106364), and UAS-mCherry-RNAi (Bloomington #35787). HaloTag-tagged UAS lines, except UAS-Myr-HaloTag, were generated in this research as described above.

7.3 Verification of LR activities associated with Myo1D and Myo1C and their derivatives tagged with HaloTag in the hindgut

To assess the LR asymmetry conferred by Myo1D, Myo1C, and their HaloTag-tagged derivatives, I conducted LR asymmetry analyses of embryonic hindguts via the misexpression of corresponding genes driven by the *byn-GAL4* under the UAS promoter control. Embryos were collected within stages 13–15, and the incidence of normal and inverted hindguts was quantified. Hindgut visualization was achieved through anti-Fasciclin3 (anti-Fas3) immunostaining or by introducing *UAS-myr-GFP-p10*. Immunostaining followed established protocols (Hozumi et al., 2006). I used a mouse anti-Fas3 antibody (diluted at 1:500, Developmental studies Hybridoma Bank 7G10) and an anti-mouse IgG-Cy3 antibody (diluted at 1:500, Jackson ImmunoResearch).

7.4 Single molecule imaging of larval macrophages

Third instar larvae were initially collected and sequentially washed: once with water, once with 80% EtOH, and twice with phosphate-buffered saline (PBS). The larvae were transferred onto a plastic plate (Falcon) containing 200 μL of PBS. Using a 0.7-mm needle (TERUMO), punctures were made, allowing macrophages to diffuse into the PBS. The macrophages present in the PBS were then transferred onto a 96-well glass-bottom plate (Greiner) and left for 5 min at room temperature to ensure adherence to the glass surface. After removing the PBS, 100 μL of a 0.04 pM TMR-direct ligand (Promega) in PBS was

added to the glass plate. Following a 1-min incubation at room temperature, the solution was aspirated, and the glass plate was rinsed twice with 200 µL PBS. Single molecule imaging was performed using a TIRFM setup (ECLIPSE Ti2-E, Nikon), which was in accordance with previously established parameters (Takebayashi et al., 2023). For each cell, single molecule imaging was performed at 45 FPS for 20 s (900 frames). The positional error of the TIRFM was assessed by tracking the TMR ligands attached to the glass bottom plate, estimating a positional error of 0.03 µm (30 nm). This error estimation was consistent with prior observations obtained using the same microscope setup (Takebayashi et al., 2023).

7.5 Single particle tracking

The acquisition of data for single molecule imaging was conducted using TIRFM, and subsequent image preprocessing was conducted manually using the Fiji GUI, followed by particle tracking with the TrackMate v7.9.2 (Ershov et al., 2022). The image preprocessing involved initiating a maximum intensity projection to visualize the outline of macrophages and manually define the region of interest (ROI) for subsequent analyses. Particle tracking was subsequently performed in TrackMate based on this previously determined ROI. The following parameters were used in TrackMate:

```
DO_SUBPIXEL_LOCALIZATION = True
RADIUS = 0.25
TARGET_CHANNEL = 1
THRESHOLD = 0.8
DO_MEDIAN_FILTERING = True
```

```
LINKING_MAX_DISTANCE = 0.72
ALLOW_TRACK_SPLITTING = False
ALLOW_TRACK_MERGING = False
ALLOW_GAP_CLOSING = False.
```

The LogDetectorFactory method was used for particle detection, while the SparseLAPTrackerFactory was used for tracking particles. To mitigate false positives, trajectories lasting fewer than 2 frames were filtered out from the analysis.

7.6 Dissociation analysis

Following particle tracking, the cumulative distribution function (CDF) of trajectory length was transformed into the survival function (1 − CDF). Estimation of the dissociation rate constant was conducted through a non-linear least squares method, presuming the sum of two exponential functions:

$$f(t) = p_1 \exp(-k_1 t) + p_2 \exp(-k_2 t), \qquad (1)$$

where t represents time in seconds, p_i signifies the weight of state i, and k_i is the dissociation rate of state i. The proportions were calculated as $p_1/(p_1 + p_2)$ and $p_2/(p_1 + p_2)$.

7.7 MSD analysis

MSD for tracked particles was calculated using the following formula:

$$\mathrm{MSD}(n\Delta t) = \{[x_i(t + n\Delta t) - x_i(t)]^2 + [y_i(t + n\Delta t) - y_i(t)]^2\}_i. \qquad (2)$$

As per Takebayashi et al., the formula uses these variables: $x_i(t)$ and $y_i(t)$ denote the xy coordinate of i-th trajectory at time t, Δt is the interval between two frames, and n is the frame number, and $\{\}_i$ is the average of i trajectories (Takebayashi et al., 2023). In the case of Myo1C-HaloTag, Iestimated the diffusion coefficient (D), confined area (L, μm), and position error (ϵ, μm) by fitting the following formula to the MSD within the range of $1 \leq n \leq 5$ (Saxton & Jacobson, 1997):

$$\mathrm{MSD}_{\mathrm{Confined}} = \frac{L^2}{3}\left[1 - \exp\left(-12\frac{Dt}{L^2}\right)\right] + 4\epsilon^2. \qquad (3)$$

The diffusion coefficient (D) and position error (ϵ) for Myo1D-HaloTag and Myr-HaloTag were determined through fitting the following formula to the MSD within the range of $1 \leq n \leq 5$.

$$\mathrm{MSD}_{\mathrm{Brownian}} = 4D\Delta t + 4\epsilon^2. \qquad (4)$$

7.8 Hidden Markov Model

Tracked particles were subjected to analysis by through HMM, which assumed a mixture of probability density functions of displacement. The probability density function of displacement is expressed by the following equation:

$$P(x\,|D, \Delta t) = \frac{x}{2D\Delta t}\exp\left(\frac{-x^2}{4D\Delta t}\right).$$

Here, x represents displacement, D signifies diffusion coefficient, and Δt denotes the frame interval. The Baum-Welch algorithm was employed to estimate the diffusion coefficients, initial probabilities of each state, and transition matrices of each diffusion state. Initial values for the diffusion coefficients were derived through the utilization of the k-means algorithm, whereas the initial values for the transition matrix and initial probabilities of each state were randomly determined. The convergence criterion for the Baum-Welch algorithm was defined when the increase in log-likelihood was $<10^{-2}$. The optimal number of diffusion states was determined using the AIC:

$$AIC_n = -2L_n + 2k_n,$$

where n is the number of diffusion states (n = 1–3), L_n denotes the log likelihood of the model calculated by the forward algorithm (Bishop, 2006; Rabiner, 1989), and k_n is the total number of parameters. Following parameter estimation by the Baum-Welch algorithm, the Viterbi algorithm was used to assign a diffusion state to displacements (Bishop, 2006; Forney, 1973).

8. References

Adams, D. S., Robinson, K. R., Fukumoto, T., Yuan, S., Albertson, R. C., Yelick, P., … Levin, M. (2006). Early, H+-V-ATPase-dependent proton flux is necessary for consistent left-right patterning of non-mammalian vertebrates. *Development*, *133*(9), 1657–1671. https://doi.org/10.1242/dev.02341

Akaike, H. (1974). A new look at the statistical model identification. *IEEE Transactions on Automatic Control*, *19*(6), 716–723. https://doi.org/10.1109/TAC.1974.1100705

Aw, S., Adams, D. S., Qiu, D., & Levin, M. (2008). *H,K-ATPase Protein Localization and Kir4.1 Function Reveal Concordance of 3 Axes During Early Determination of Left-Right Asymmetry*. *49*(18), 1841–1850. https://doi.org/10.1016/j.jacc.2007.01.076.White

Babu, D., & Roy, S. (2013). Left–right asymmetry: Cilia stir up new surprises in the node. *Open Biology*, *3*(5), 130052. https://doi.org/10.1098/rsob.130052

Báez-Cruz, F. A., & Ostap, E. M. (2023). Drosophila class-I myosins that can impact left-right asymmetry have distinct ATPase kinetics. *Journal of Biological Chemistry*, *299*(8), 104961. https://doi.org/10.1016/j.jbc.2023.104961

Bateman, J. R., Lee, A. M., & Wu, C. (2006). Site-Specific Transformation of Drosophila via *φ*C31 Integrase-Mediated Cassette Exchange. *Genetics*, *173*(2), 769–777. https://doi.org/10.1534/genetics.106.056945

Bishop, C. M. (2006). *Pattern recognition and machine learning*. Springer.

Cheng, C., D.Little, C., & J.Rongish, B. (2009). Rotation of organiser tissue contributes to left-right asymmetry. *NIH Public Access*, *292*(4), 557–561. https://doi.org/10.1002/ar.20872.Rotation

Cho, B., Yoon, S.-H., Lee, D., Koranteng, F., Tattikota, S. G., Cha, N., … Shim, J. (2020). Single-cell transcriptome maps of myeloid blood cell lineages in Drosophila. *Nature Communications*, *11*(1), 4483. https://doi.org/10.1038/s41467-020-18135-y

Chougule, A., Lapraz, F., Földi, I., Cerezo, D., Mihály, J., & Noselli, S. (2020). The Drosophila actin nucleator DAAM is essential for left-right asymmetry. *PLOS Genetics*, *16*(4), e1008758. https://doi.org/10.1371/journal.pgen.1008758

Coutelis, J.-B., Géminard, C., Spéder, P., Suzanne, M., Petzoldt, A. G., & Noselli, S. (2013). Drosophila Left/Right Asymmetry Establishment Is Controlled by the Hox Gene Abdominal-B. *Developmental Cell*, *24*(1), 89–97. https://doi.org/10.1016/j.devcel.2012.11.013

Davison, A., McDowell, G. S., Holden, J. M., Johnson, H. F., Koutsovoulos, G. D., Liu, M. M., … Blaxter, M. L. (2016). Formin Is Associated with Left-Right Asymmetry in the Pond Snail and the Frog. *Current Biology*, *26*(5), 654–660. https://doi.org/10.1016/j.cub.2015.12.071

Ershov, D., Phan, M.-S., Pylvänäinen, J. W., Rigaud, S. U., Le Blanc, L., Charles-Orszag, A., … Tinevez, J.-Y. (2022). TrackMate 7: Integrating state-of-the-art segmentation algorithms into tracking pipelines. *Nature Methods*, *19*(7), 829–832. https://doi.org/10.1038/s41592-022-01507-1

Fan, J., Ray, P., Lu, Y., Kaur, G., Schwarz, J. J., & Wan, L. Q. (2018). Cell chirality regulates intercellular junctions and endothelial permeability. *Science Advances*, *4*(10), eaat2111. https://doi.org/10.1126/sciadv.aat2111

Forney, G. D. (1973). The viterbi algorithm. *Proceedings of the IEEE*, *61*(3), 268–278. https://doi.org/10.1109/PROC.1973.9030

Golan, Y., & Sherman, E. (2017). Resolving mixed mechanisms of protein subdiffusion at the T cell plasma membrane. *Nature Communications*, *8*. https://doi.org/10.1038/ncomms15851

Grand, C., Martín-Durán, J. M., Kenny, N. J., Truchado-García, M., & Hejnol, A. (2014). Evolution, divergence and loss of the nodal signalling pathway: New data and a synthesis across the Bilateria. *The International Journal of Developmental Biology*, *58*(6-7-8), 521–532. https://doi.org/10.1387/ijdb.140133cg

Gros, J., Feistel, K., Viebahn, C., Blum, M., & Tabin, C. J. (2009). Cell Movements at Hensen's Node Establish Left/Right Asymmetric Gene Expression in the Chick. *Science*, *324*(5929), 941–944. https://doi.org/10.1126/science.1172478

Hatori, R., Ando, T., Sasamura, T., Nakazawa, N., Nakamura, M., Taniguchi, K., … Matsuno, K. (2014). Left-right asymmetry is formed in individual cells by intrinsic cell chirality. *Mechanisms of Development*, *133*, 146–162. https://doi.org/10.1016/j.mod.2014.04.002

Hibino, T., Ishii, Y., Levin, M., & Nishino, A. (2006). Ion flow regulates left–right asymmetry in sea urchin development. *Development Genes and Evolution*, *216*(5), 265. https://doi.org/10.1007/s00427-005-0051-6

Hozumi, S., Maeda, R., Taniguchi, K., Kanai, M., Shirakabe, S., Sasamura, T., … Matsuno, K. (2006). An unconventional myosin in Drosophila reverses the default handedness in visceral organs. *Nature*, *440*(7085), 798–802. https://doi.org/10.1038/nature04625

Hozumi, S., Maeda, R., Taniguchi-Kanai, M., Okumura, T., Taniguchi, K., Kawakatsu, Y., … Matsuno, K. (2008). Head region of unconventional myosin I family members is responsible for the organ-specificity of their roles in left-right polarity in Drosophila. *Developmental Dynamics*, *237*(12), 3528–3537. https://doi.org/10.1002/dvdy.21583

Inaki, M., Liu, J., & Matsuno, K. (2016). Cell chirality: Its origin and roles in left–right asymmetric development. *Philosophical Transactions of the Royal Society B: Biological Sciences*, *371*(1710), 20150403. https://doi.org/10.1098/rstb.2015.0403

Ishibashi, T., Hatori, R., Maeda, R., Nakamura, M., Taguchi, T., Matsuyama, Y., & Matsuno, K. (2019). E and ID proteins regulate cell chirality and left-right asymmetric

development in *Drosophila*. *Genes to Cells*, *24*(3), 214–230. https://doi.org/10.1111/gtc.12669

Ishibashi, T., Inaki, M., & Matsuno, K. (2020). Statistical Validation Verifies That Enantiomorphic States of Chiral Cells Are Determinant Dictating the Left- or Right-Handed Direction of the Hindgut Rotation in Drosophila. *Symmetry*, *12*(12), 1991. https://doi.org/10.3390/sym12121991

Iwaki, D. D., & Lengyel, J. A. (2002). A Delta–Notch signaling border regulated by Engrailed/Invected repression specifies boundary cells in the Drosophila hindgut. *Mechanisms of Development*, *114*(1), 71–84. https://doi.org/10.1016/S0925-4773(02)00061-8

Janczura, J., Balcerek, M., Burnecki, K., Sabri, A., Weiss, M., & Krapf, D. (2021). Identifying heterogeneous diffusion states in the cytoplasm by a hidden Markov model. *New Journal of Physics*, *23*(5), 053018. https://doi.org/10.1088/1367-2630/abf204

Kochubey, O., Majumdar, A., & Klingauf, J. (2006). Imaging Clathrin Dynamics in Drosophila melanogaster Hemocytes Reveals a Role for Actin in Vesicle Fission. *Traffic*, *7*(12), 1614–1627. https://doi.org/10.1111/j.1600-0854.2006.00492.x

Kohl, J., Ng, J., Cachero, S., Ciabatti, E., Dolan, M.-J., Sutcliffe, B., … Jefferis, G. S. X. E. (2014). Ultrafast tissue staining with chemical tags. *Proceedings of the National Academy of Sciences*, *111*(36), E3805–E3814. https://doi.org/10.1073/pnas.1411087111

Kramer-Zucker, A. G. (2005). Cilia-driven fluid flow in the zebrafish pronephros, brain and Kupffer's vesicle is required for normal organogenesis. *Development*, *132*(8), 1907–1921. https://doi.org/10.1242/dev.01772

Kuroda, R., Endo, B., Abe, M., & Shimizu, M. (2009). Chiral blastomere arrangement dictates zygotic left–right asymmetry pathway in snails. *Nature*, *462*(7274), 790–794. https://doi.org/10.1038/nature08597

Lebreton, G., Géminard, C., Lapraz, F., Pyrpassopoulos, S., Cerezo, D., Spéder, P., … Noselli, S. (2018). Molecular to organismal chirality is induced by the conserved myosin 1D. *Science*, *362*(6417), 949–952. https://doi.org/10.1126/science.aat8642

Levin, M., Thorlin, T., Robinson, K. R., Nogi, T., & Mercola, M. (2002). Asymmetries in H+/K+-ATPase and Cell Membrane Potentials Comprise a Very Early Step in Left-Right Patterning. *Cell*, *111*(1), 77–89. https://doi.org/10.1016/S0092-8674(02)00939-X

Loffreda, A., Jacchetti, E., Antunes, S., Rainone, P., Daniele, T., Morisaki, T., … Mazza, D. (2017). Live-cell P53 single-molecule binding is modulated by C-terminal acetylation and correlates with transcriptional activity. *Nature Communications*, *8*(1), 313. https://doi.org/10.1038/s41467-017-00398-7

Matsuoka, S., Shibata, T., & Ueda, M. (2013). Asymmetric PTEN Distribution Regulated by Spatial Heterogeneity in Membrane-Binding State Transitions. *PLoS Computational Biology*, *9*(1), e1002862. https://doi.org/10.1371/journal.pcbi.1002862

McIntosh, B. B., & Ostap, E. M. (2016). Myosin-I molecular motors at a glance. *Journal of Cell Science*, *129*(14), 2689–2695. https://doi.org/10.1242/jcs.186403

Mech, L. D. (2014). Body Handedness Is Directed by Genetically Determined Cytoskeletal Dynamics in the Early Embryo. *Canadian Field-Naturalist*, *128*(2), 189–190. https://doi.org/10.1016/j

Michalet, X. (2010). Mean square displacement analysis of single-particle trajectories with localization error: Brownian motion in an isotropic medium. *Physical Review E - Statistical, Nonlinear, and Soft Matter Physics*, *82*(4), 1–13. https://doi.org/10.1103/PhysRevE.82.041914

Morgan, N. S., Skovronsky, D. M., Artavanis-Tsakonas, S., & Mooseker, M. S. (1994). The Molecular Cloning and Characterization of Drosophila melanogaster Myosin-IA and Myosin-IB. *Journal of Molecular Biology*, *239*(3), 347–356. https://doi.org/10.1006/jmbi.1994.1376

Motohashi, K. (2015). A simple and efficient seamless DNA cloning method using SLiCE from Escherichia coli laboratory strains and its application to SLiP site-directed mutagenesis. *BMC Biotechnology*, *15*(1), 47. https://doi.org/10.1186/s12896-015-0162-8

Nonaka, S., Shiratori, H., Saijoh, Y., & Hamada, H. (2002). Determination of left–right patterning of the mouse embryo by artificial nodal flow. *Nature*, *418*(6893), 96–99. https://doi.org/10.1038/nature00849

Nonaka, S., Tanaka, Y., Okada, Y., Takeda, S., Harada, A., Kanai, Y., … Hirokawa, N. (1998). Randomization of left-right asymmetry due to loss of nodal cilia generating leftward flow of extraembryonic fluid in mice lacking KIF3B motor protein. *Cell*, *95*(6), 829–837. https://doi.org/10.1016/S0092-8674(00)81705-5

Rabiner, L. R. (1989). A tutorial on hidden Markov models and selected applications in speech recognition. *Proceedings of the IEEE*, *77*(2), 257–286. https://doi.org/10.1109/5.18626

Sabri, A., Xu, X., Krapf, D., & Weiss, M. (2020). Elucidating the Origin of Heterogeneous Anomalous Diffusion in the Cytoplasm of Mammalian Cells. *Physical Review Letters*, *125*(5), 058101. https://doi.org/10.1103/PhysRevLett.125.058101

Sampson, C. J., Amin, U., & Couso, J.-P. (2013). Activation of Drosophila hemocyte motility by the ecdysone hormone. *Biology Open*, *2*(12), 1412. https://doi.org/10.1242/bio.20136619

Sato, K., Hiraiwa, T., Maekawa, E., Isomura, A., Shibata, T., & Kuranaga, E. (2015). Left-right asymmetric cell intercalation drives directional collective cell movement in epithelial morphogenesis. *Nature Communications*, *6*, 1–11. https://doi.org/10.1038/ncomms10074

Saxton, M. J., & Jacobson, K. (1997). Single-particle tracking: Applications to membrane dynamics. *Annual Review of Biophysics and Biomolecular Structure*, *26*, 373–399. https://doi.org/10.1146/annurev.biophys.26.1.373

Schweickert, A., Weber, T., Beyer, T., Vick, P., Bogusch, S., Feistel, K., & Blum, M. (2007). Cilia-Driven Leftward Flow Determines Laterality in Xenopus. *Current Biology*, *17*(1), 60–66. https://doi.org/10.1016/j.cub.2006.10.067

Shimeld, S. M., & Levin, M. (2006). Evidence for the regulation of left-right asymmetry inCiona intestinalis by ion flux. *Developmental Dynamics*, *235*(6), 1543–1553. https://doi.org/10.1002/dvdy.20792

Spéder, P., Ádám, G., & Noselli, S. (2006). Type ID unconventional myosin controls left–right asymmetry in Drosophila. *Nature*, *440*(7085), 803–807. https://doi.org/10.1038/nature04623

Stephen, L. A., Johnson, E. J., Davis, G. M., McTeir, L., Pinkham, J., Jaberi, N., & Davey, M. G. (2014). The chicken left right organizer has nonmotile cilia which are lost in a stage-dependent manner in the *Talpid* ^{3} ciliopathy. *Genesis*, *52*(6), 600–613. https://doi.org/10.1002/dvg.22775

Takebayashi, K., Kamimura, Y., & Ueda, M. (2023). Field model for multistate lateral diffusion of various transmembrane proteins observed in living *Dictyostelium* cells. *Journal of Cell Science*, *136*(4), jcs260280. https://doi.org/10.1242/jcs.260280

Tamada, A., Kawase, S., Murakami, F., & Kamiguchi, H. (2010). Autonomous right-screw rotation of growth cone filopodia drives neurite turning. *The Journal of Cell Biology*, *188*(3), 429–441. https://doi.org/10.1083/jcb.200906043

Taniguchi, K., Maeda, R., Ando, T., Okumura, T., Nakazawa, N., Hatori, R., … Matsuno, K. (2011). Chirality in Planar Cell Shape Contributes to Left-Right Asymmetric Epithelial Morphogenesis. *Science*, *333*(6040), 339–341. https://doi.org/10.1126/science.1200940

Tee, Y. H., Goh, W. J., Yong, X., Ong, H. T., Hu, J., Tay, I. Y. Y., … Bershadsky, A. D. (2023). Actin polymerisation and crosslinking drive left-right asymmetry in single cell and cell collectives. *Nature Communications*, *14*(1), 776. https://doi.org/10.1038/s41467-023-35918-1

Tee, Y. H., Shemesh, T., Thiagarajan, V., Hariadi, R. F., Anderson, K. L., Page, C., … Bershadsky, A. D. (2015). Cellular chirality arising from the self-organization of the actin cytoskeleton. *Nature Cell Biology*, *17*(4), 445–457. https://doi.org/10.1038/ncb3137

Ueda, M., Sako, Y., Tanaka, T., Devreotes, P., & Yanagida, T. (2001). Single-Molecule Analysis of Chemotactic Signaling in Dictyostelium Cells. *Science*, *294*(5543), 864–867. https://doi.org/10.1126/science.1063951

Wan, L. Q., & Vunjak-novakovic, G. (2011). *Micropatterning chiral morphogenesis*. (December), 745–748. https://doi.org/10.4161/cib.4.6.17649

Wood, W. B. (1991). Evidence from reversal of handedness in C. Elegans embryos for early cell interactions determining cell fates. *Nature*, *349*(6309), 536–538. https://doi.org/10.1038/349536a0

Xu, J., Van Keymeulen, A., Wakida, N. M., Carlton, P., Berns, M. W., & Bourne, H. R. (2007). Polarity reveals intrinsic cell chirality. *Proceedings of the National Academy of Sciences of the United States of America*, *104*(22), 9296–9300. https://doi.org/10.1073/pnas.0703153104

Yamanaka, H., & Kondo, S. (2015). Rotating pigment cells exhibit an intrinsic chirality. *Genes to Cells*, *20*(1), 29–35. https://doi.org/10.1111/gtc.12194

Yanagawa, M., Hiroshima, M., Togashi, Y., Abe, M., Yamashita, T., Shichida, Y., … Sako, Y. (2018). Single-molecule diffusion-based estimation of ligand effects on G protein–coupled receptors. *Science Signaling*, *11*(548), eaao1917. https://doi.org/10.1126/scisignal.aao1917

Yoshiba, S., Shiratori, H., Kuo, I. Y., Kawasumi, A., Shinohara, K., Nonaka, S., … Hamada, H. (2012). Cilia at the Node of Mouse Embryos Sense Fluid Flow for Left-Right Determination via Pkd2. *Science*, *338*(6104), 226–231. https://doi.org/10.1126/science.1222538

Yoshioka, D., Fukushima, S., Koteishi, H., Okuno, D., Ide, T., Matsuoka, S., & Ueda, M. (2020). Single-molecule imaging of PI(4,5)P2 and PTEN in vitro reveals a positive feedback mechanism for PTEN membrane binding. *Communications Biology*, *3*(1), 1–14. https://doi.org/10.1038/s42003-020-0818-3

Zettervall, C.-J., Anderl, I., Williams, M. J., Palmer, R., Kurucz, E., Ando, I., & Hultmark, D. (2004). A directed screen for genes involved in Drosophila blood cell activation. *Proceedings of the National Academy of Sciences*, *101*(39), 14192–14197. https://doi.org/10.1073/pnas.0403789101

9. Acknowledgements

I would like to express my deepest gratitude to supervisor Professor Kenji Matsuno, whose guidance, support, and insightful discussion throughout this research. Your wisdom, knowledge, commitment, and positiveness inspired me greatly. I am immensely thankful to my collaborators, Kazutoshi Takebayashi and Professor Masahiro Ueda, for their invaluable contributions to this thesis and sharing their expertise and resources. Their perspectives and expertise enriched this work in countless ways. I would also like to express my deepest appreciation to Professor Masahiro Ueda and Professor Kon Takahide for participating in the degree examination and providing valuable advice. I thank to the members of Laboratory of Cell Biology for providing great advice for this research. Additionally, Ms. Asuka Yamaguchi provided support for preparing *Drosophila* strains for the experiment. Dr. Takeshi Sasamura and Dr. Mikiko Inaki shared me their knowledge throughout the research. I express my deepest gratitude here. Finally, I want to thank my family and friends. I could not have continued my research without their support. Thank you.

10. Publication lists

Sosuke, U., Kazutoshi, T., Asuka, Y., Takeshi, S., Mikiko, I., Masahiro, U., & Kenji. M. (2024). Left-right Myosin-Is, Myosin1C, and Myosin1D exhibit distinct single molecule behaviors on the plasma membrane of *Drosophila* macrophages. *Genes to Cells, in press*